UNIVERSITY OF CALIFORNIA SAN DIEGO

Excitonic Devices and Transport Properties

A dissertation submitted in partial satisfaction of the
requirements for the degree
Doctor of Philosophy

in

Physics

by

Chelsey Jane Dorow

Committee in charge:

Professor Leonid Butov, Chair
Professor Misha Fogler
Professor Brian Maple
Professor Shayan Mookherjea
Professor Stojan Radic

2019

The dissertation of Chelsey Jane Dorow is approved, and it is acceptable in quality and form for publication on microfilm and electronically:

_____

_____

_____

_____

_____

Chair

University of California San Diego

2019

EPIGRAPH

I have no dress except the one I wear every day. If you are going to be kind enough to give me one, please let it be practical and dark so that I can put it on afterwards to go to the laboratory.

— Marie Curie

TABLE OF CONTENTS

LIST OF FIGURES

ACKNOWLEDGEMENTS

First, I would like to thank my advisor, Professor Leonid Butov, for guidance during my PhD research and for teaching many important lessons about performing careful, rigorous experimental work. Leonid has developed a versatile, far-reaching research program which has given me many diverse learning opportunities, inside and outside of academia. I'm grateful to have had this environment to explore my career ambitions.

I would also like to thank many coworkers. Erica Calman and Matt Hasling taught me many things over the years and provided a lot of humor to get through the day to day challenges of experimental work. I am thankful to Yuliya Kuznetsova for training me and for providing priceless career advice and encouragement. I would like to thank Jason Leonard for adding calculations to my experimental work and for helping me study for my qualifying exam. I am thankful to Darius Choksy and Lewis Fowler-Gerace for taking on the next generation of Butov group experiments.

I am grateful to Joe Wilkes and Misha Fogler for insightful theoretical contributions. I am thankful to the groups of Art Gossard and Loren Pfeiffer for providing very high-quality samples for my experiments.

I would like to thank Jacqueline Bloch and Alberto Amo for welcoming me into their research group. My research stay in France was a very interesting and memorable part of my time in graduate school.

I would like to thank my undergraduate research advisor, Professor Martin Greven, for giving me so many opportunities and challenging me as a young scientist. I am also grateful to Dr. Mun Chan who taught me how to be effective as a researcher. The work I did with the Greven group inspired me to get a PhD in physics.

Finally, I would like to thank all my family and friends for all of their support. My parents and siblings have always provided a lot of encouragement, even though they have no idea what I'm working on. I would like to thank Olivia for brightening this San Diego adventure, and I

would like to thank Taryn for sticking with me since the days I was taking first-year physics in Tate Hall.

The text of chapter 3, in part, is a reprint of the material as it appears in C. J. Dorow, M. W. Hasling, E. V. Calman, L. V. Butov, J. Wilkes, K. L. Campman, and A. C. Gossard, Spatially resolved and time-resolved imaging of transport of indirect excitons in high magnetic fields. *Physical Review B* 95, 235308 (2017), ©2017 American Physical Society, where the dissertation author was the first author. The co-authors in these publications directed, supervised, and co-worked on the research which forms the basis of this chapter.

The text of chapter 4, in part, is a reprint of the material as it appears in C. J. Dorow, Y. Y. Kuznetsova, J. R. Leonard, M. K. Chu, L. V. Butov, J. Wilkes, M. Hanson, and A. C. Gossard, Indirect excitons in a potential energy landscape created by a perforated electrode. *Applied Physics Letters* 108, 073502 (2016), ©2016 AIP Publishing LLC, where the dissertation author was the first author. The co-authors in these publications directed, supervised, and co-worked on the research which forms the basis of this chapter.

The text of chapter 5, in part, is a reprint of the material as it appears in C. J. Dorow, J. R. Leonard, M. M. Fogler, L. V. Butov, K. W. West, and L. N. Pfeiffer, Split-gate device for indirect excitons, *Applied Physics Letters* 112, 183501 (2018), ©2018 AIP Publishing LLC, where the dissertation author was the first author. The co-authors in these publications directed, supervised, and co-worked on the research which forms the basis of this chapter.

The text of chapter 6, in part, is a reprint of the material as it appears in C. J. Dorow, M. W. Hasling, D. J. Choksy, J. R. Leonard, L. V. Butov, K. W. West, and L. N. Pfeiffer, High-mobility indirect excitons in wide single quantum well, *Applied Physics Letters* 113, 212102 (2018), ©2018 AIP Publishing LLC, where the dissertation author was the first author. The co-authors in these publications directed, supervised, and co-worked on the research which forms the basis of this chapter.

VITA

2013	B.S. in Physics, College of Science and Engineering, University of Minnesota, Twin Cities
2013 - 2014	Graduate Teaching Assistant, Department of Physics, University of California, San Diego
2015	M.S. in Physics, Department of Physics, University of California, San Diego
2015 - 2018	Graduate Research Fellow, National Science Foundation
Fall 2017	Visiting Scientist, Center for Nanoscience and Nanotechnology, Palaiseau, France
Summer 2018	Device Characterization Intern, Micron Technology, Boise, Idaho
2019	Ph.D. in Physics, Department of Physics, University of California, San Diego

PUBLICATIONS

C. J. Dorow, M. W. Hasling, D. J. Choksy, J. R. Leonard, L. V. Butov, K. W. West, L. N. Pfeiffer. High-mobility indirect excitons in wide single quantum well. *Applied Physics Letters* 113, 212102 (2018)

C. J. Dorow, J. R. Leonard, L. V. Butov, K. W. West, L. N. Pfeiffer. Split-gate device for indirect excitons. *Applied Physics Letters* 112, 183501 (2018)

C. J. Dorow, M. W. Hasling, E. V. Calman, L. V. Butov, J. Wilkes, K. L. Campman, and A. C. Gossard. Spatially and time-resolved imaging of transport of indirect excitons in high magnetic fields. *Physical Review B* 95, 235308 (2017)

Y. Y. Kuznetsova, C. J. Dorow, E. V. Calman, L. V. Butov, J. Wilkes, K. L. Campman, A. C. Gossard. Transport of indirect excitons in high magnetic fields. *Physical Review B* 95, 125304 (2017)

C. J. Dorow, Y. Y. Kuznetsova, J. R. Leonard, M. K. Chu, L. V. Butov, J. Wilkes, M. Hanson, A. C. Gossard. Indirect excitons in a potential energy landscape created by a perforated electrode. *Applied Physics Letters* 108, 073502 (2016)

E. V. Calman, C. J. Dorow, M. M. Fogler, L. V. Butov, S. Hu, A. Mishchenko, A. K. Geim. Control of excitons in multi-layer van der Waals heterostructures. *Applied Physics Letters* 108, 101901 (2016)

M. Remeika, J. R. Leonard, C. J. Dorow, M. M. Fogler, L. V. Butov, M. Hanson, A. C. Gossard. Measurement of exciton interaction using electrostatic lattice. *Physical Review B* 92, 115311 (2015)

M. W. Hasling, Y. Y. Kuznetsova, P. Andreakou, J. R. Leonard, E. V. Calman, C. J. Dorow, L. V. Butov, M. Hanson, A. C. Gossard. Stirring potential for indirect excitons. *Journal of Applied Physics* 117, 023108 (2015)

Y. Tang, L. Mangin-Thro, A. Wildes, M. K. Chan, C. J. Dorow, J. Jeong, Y. Sidis, M. Greven, P. Bourges. Orientation of the intra-unit-cell magnetic moment in the high-T_c superconductor $HgBa_2CuO_{4+\delta}$. *Physical Review B* 98, 214418 (2018)

M. K. Chan, Y. Tang, C. J. Dorow, J. Jeong, L. Mangin-Thro, M. J. Veit, Y. Ge, D. L. Abernathy, Y. Sidis, P. Bourges, M. Greven. Hourglass Dispersion and Resonance of Magnetic Excitations in the Superconducting State of the Single-Layer Cuprate $HgBa_2CuO_{4+\delta}$ Near Optimal Doping. *Physical Review Letters* 117, 277002 (2016)

J. P. Hinton, L. Kemper, E. Thewalt, Z. Alpichshev, M. Veit, C. Dorow, L. Ji, N. Barišić, N. Gedik, M. Greven, J. D. Koralek, M. K. Chan, J. Orenstein. Quasiparticle recombination and coherence near T_c in the $HgBa_2CuO_{4+\delta}$ cuprate superconductor. *Scientific Reports* 6, 23610 (2016)

M. K. Chan, C. Dorow, L. Mangin-Thro, Y. Tang, M. Veit, Y. Ge, J. T. Park, A. D. Christianson, P. Steffens, Y. Sidis, X. Zhao, D. L. Abernathy, P. Bourges, M. Greven. Commensurate antiferromagnetic fluctuations as a signature of the pseudogap in a model cuprate. *Nature Communications* 7, 10819 (2016)

N. Barišić, M. K. Chan, M. J. Veit, C. J. Dorow, Y. Ge, Y. Tang, W. Tabiś, G. Yu, X. Zhao, M. Greven. Hidden Fermi-liquid behavior throughout the phase diagram of the cuprates. arXiv: 1507.07885 (2015)

D. Rybicki, J. Kohlrautz, J. Haase, M. Greven, G. Yu, Y. Li, X. Zhao, C. Dorow, M. Veit. Components of the uniform magnetic susceptibility in $HgBa_2CuO_{4+\delta}$ from ^{63}Cu nuclear magnetic resonance. *Physical Review B* 92, 081115 (2015)

M. K. Chan, M. Veit, C. Dorow, Y. Ge, W. Tabiś, B. Vignolle, X. Zhao, C. Proust, N. Barišić, M. Greven. In-plane magnetoresistance obeys Kohler's rule in the pseudogap phase of cuprate superconductors. *Physical Review Letters* 113, 177005 (2014)

F. Cilento, S. Dal Conte, G. Coslovich, S. Peli, N. Nembrini, S. Mor, F. Banfi, G. Ferrini, H. Eisaki, M. K. Chan, C. J. Dorow, M. J. Veit, M. Greven, D. van der Marel, R. Comin, A. Damascelli, L. Rettig, U. Bovensiepen, M. Capone, C. Giannetti, F. Parmigiani. Photo-enhanced antinodal conductivity in the pseudogap state of high-T_c cuprates. *Nature Communications* 5, 4353 (2014)

W. Tabiś, Y. Li, M. Le Tacon, L. Braicovich, A. Kreyssig, M. Minola, G. Dellea, E. Weschke, M. Veit, A. Goldman, T. Schmitt, G. Ghiringhelli, N. Barišić, M. K. Chan, C. Dorow, G. Yu, X. Zhao, B. Keimer M. Greven. Universal bulk charge-density-wave correlations in the cuprate superconductors. *Nature Communications* 5, 5875 (2014)

S. Wang, J. Zhang, J. Yan, X. J. Chen, V. Struzhkin, W. Tabiś, N. Barišić, M. Chan, C. Dorow, X. Zhao, M. Greven, W. L. Mao, T. Geballe. The strain derivatives of T_c in $HgBa_2CuO_{4+\delta}$: CuO_2 plane alone is not enough. *Physical Review B* 89, 024515 (2014)

N. Barišić, S. Badoux, M. K. Chan, C. Dorow, W. Tabiś, B. Vignolle, G. Yu, J. Béard, X. Zhao, C. Proust, M. Greven. Universal quantum oscillations in the underdoped cuprate superconductors. *Nature Physics* 9, 761 (2013)

A. M. Mounce, S. Oh, J. A. Lee, W. P. Halperin, A. P. Reyes, P. L. Kuhns, M. K. Chan, C. Dorow, L. Ji, D. Xia, X. Zhao, M. Greven. Absence of static loop-current magnetism at the apical oxygen site in $HgBa_2CuO_{4+\delta}$ from NMR. *Physical Review Letters* 111, 187003 (2013)

Y. Li, M. Le Tacon, Y. Matiks, A. V. Boris, T. Loew, C. T. Lin, Lu Chen, M. K. Chan, C. Dorow, L. Ji, N. Barišić, X. Zhao, M. Greven, B. Keimer. Doping-dependent photon scattering resonance in the model high-temperature superconductor $HgBa_2CuO_{4+\delta}$ revealed by raman scattering and optical ellipsometry. *Physical Review Letters* 111, 187001 (2013)

ABSTRACT OF THE DISSERTATION

Excitonic Devices and Transport Properties

by

Chelsey Jane Dorow

Doctor of Philosophy in Physics

University of California San Diego, 2019

Professor Leonid Butov, Chair

Over several decades, research in semiconductor physics has revealed a rich plethora of physical phenomena filled with electric, magnetic, and optical processes for physicists and engineers to observe and manipulate. In addition to hosting a number of fundamental discoveries in physics, several of which merited Nobel Prizes, semiconductor physics has also revolutionized modern technology, most notably in the field of computing.

An especially interesting topic in this field is the physics of quasiparticles, which are excitations or disturbances in matter that resemble particles in free space. This dissertation focuses on excitons, which are quasiparticles that exist in semiconductor materials and are a bound state of an electron and a hole. Excitons can interact with light, either through their photo-generation

or by radiative recombination of the electron and hole, and therefore can aid in the study of the interaction of light and matter.

This dissertation in particular looks at a specially engineered system of excitons: indirect excitons in coupled quantum wells. In this system, the electron and hole of the exciton are confined to two separate quantum well layers and are, as a result, separated in space, typically by ~ 10 nm, depending on the coupled quantum well structure.

Indirect excitons possess several unique properties including a built-in electric dipole moment, long lifetimes, energy control by applied voltage, and the ability to form a quantum Bose gas, making them a useful system to study fundamental physics of cold bosons and to investigate ways to integrate these properties into modern day technology. The experiments detailed in this dissertation probe the basic physics of exciton transport in high magnetic fields and expand upon our current understanding of how nano-scale devices can be used to control electronic and optical processes in solids.

Chapter 1

Introduction to Indirect Excitons

Excitons are quasiparticles, first predicted by Frenkel in 1931 [1, 2], that are composed of a bound electron and hole. Excitons provide a unique opportunity in condensed matter physics to study the interaction of light and matter and to observe properties and phenomena of bosons in solid-state systems, including Bose-Einstein condensation at temperatures several orders of magnitude higher than atomic condensate temperatures [3]. Furthermore, excitonic devices are being developed as an alternative to electronic devices for applications in excitonic signal processing with efficient coupling to optical communication [4].

1.1 Indirect excitons in coupled quantum wells

The work discussed in this thesis is based on experiments performed on a specially engineered excitonic system: indirect excitons in coupled quantum wells (CQWs). An indirect exciton (IX) is a bound electron and hole that are spatially confined in two separate quantum wells and exist in layered semiconductor structures as shown in Figure 1.1(a). As a result of the QW confinement, the electron and hole are spatially separated, typically by $\sim$10 nm, but the separation distance depends on sample geometry. One common quantum well layered semiconductor structure involves GaAs quantum wells with an AlGaAs barrier; such structures are used in the

experiments of this dissertation. The GaAs and AlGaAs system is desirable due to the direct band gap of GaAs, high-quality interfaces of GaAs/AlGaAs that are possible in molecular beam epitaxial growth, and low defect density, which gives high carrier mobilities.

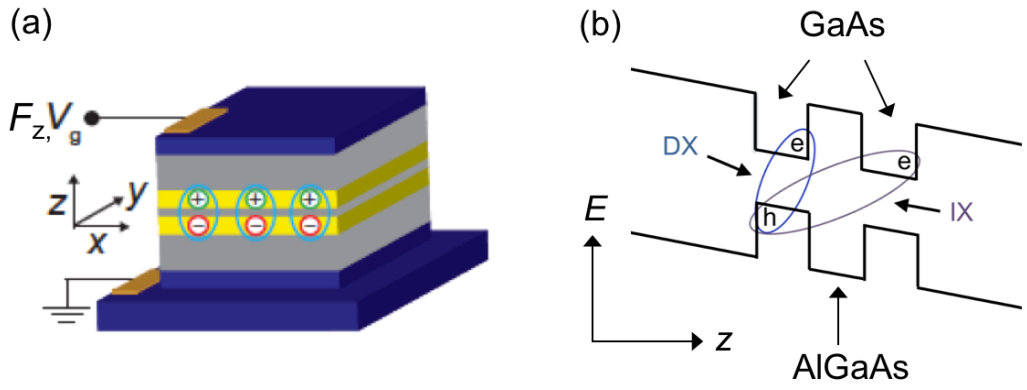

Figure 1.1: (a) Layered semiconductor QW structure (QW in yellow). Voltage applied to gates achieves the IX regime. (b) CQW energy band diagram with applied voltage.

Electrons and holes are excited in the system with laser excitation, and a gate voltage applied perpendicular to the quantum well plane enables the realization of the indirect regime, which is the regime in which the IX is the lowest exciton energy state, as opposed to the direct exciton (DX): an exciton composed of an electron and hole in the same quantum well layer. The indirect regime is achieved as follows. The energy of a DX is $E_{DX} = E_g - E_{b,DX}$, where E_g is the band gap energy ($\sim$ 1.5 eV for GaAs) and $E_{b,DX}$ is the DX binding energy ($\sim$ 10 meV for typical CQW GaAs structures). The energy of the IX is $E_{IX} = E_g - E_{b,IX} - edF_z$, where $E_{b,IX}$ is now the IX binding energy of $\sim$ 5 meV for an electron and hole in two separate QW layers, e is the electron charge, d is approximately the distance between QW centers, and F_z is the applied electric field. When a strong enough electric field is applied such that $edF_z \geq E_{b,DX} - E_{b,IX}$, then the IX becomes the lowest energy exciton. The band diagram is shown in Figure 1.1(b). Figure 1.2 shows data demonstrating the DX to IX crossover with applied gate voltage [5, 6].

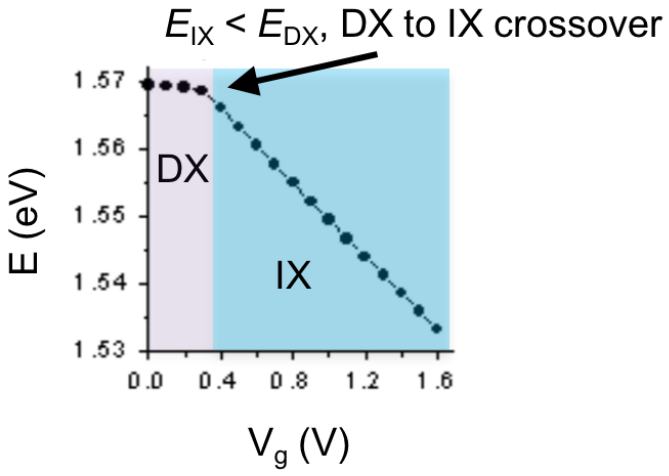

Figure 1.2: Data [5] showing exciton energy vs applied gate voltage, V_g. With high enough V_g, the IX energy becomes the lowest exciton energy state and there is a crossover from DX to IX.

1.2 Useful properties of indirect excitons

The IX system is used because it provides several advantageous properties that enable fundamental physics studies and the development of excitonic devices. Some of these useful properties are described below.

i. Long and controllable indirect exciton lifetimes

The radiative recombination rate of excitons is inversely proportional to the overlap of the electron and hole wavefunctions squared. Therefore, due to the spatial separation of the electrons and holes and the QW barrier, IXs may have lifetimes that exceed tens of μs, several orders of magnitude longer than the lifetime of DXs, which is typically on the order of tens of ps. Additionally, the IX lifetime is controllable by gate voltage [7].

ii. Disorder screening

Since IXs form oriented dipoles as seen in Figure 1.1, they experience repulsive interactions. Repulsive interactions can facilitate disorder screening and aid in the achievement of long-range IX transport [9]. This effect is visible in an IX localization-delocalization transition

observed when IXs effectively screen out disorder at higher IX densities [58].

iii. Long-range transport

The long IX lifetimes in addition to the efficient disorder screening enables IXs to travel large distances before recombination. The IX transport distance can reach up to hundreds of microns [10, 11, 12].

iv. Control of indirect exciton energy by voltage

The oriented dipole character of IXs can be exploited to control their energy with gate voltage [13, 14]. A gate voltage applied perpendicular to the QW planes will shift the energy by $U = edF_z$ where e is the electron charge, d is approximately the distance between the QW centers and F_z is the normal component of the electric field. The control of the IX energy by voltage in this way enables the versatile creation of potential energy landscapes of virtually any energy profile where the potential landscape is $U(x,y) = edF_z(x,y)$. Electrodes have been carefully patterned to realize several types of excitonic devices with applications for fundamental physics studies such as excitonic traps, lattices, conveyers, and stirring potentials and for circuit applications such as excitonic transistors, ramps and photon storage devices [4]. A description of excitonic device fabrication is presented in Section 2.3.

v. Fast cooling rates of indirect excitons

Efficient cooling is present in the IX system. As the IXs consist of an electron and hole confined to quantum wells, a relaxation of momentum conservation in the z-direction (confinement direction) occurs. IXs cool through emission of phonons, and the momentum conservation relaxation increases the rate of phonon emission. The cooling rate for the IXs in GaAs CQW structures is about three times higher than for excitons in bulk GaAs [6, 16, 17, 18].

The IX system provides a few other advantages in addition to these listed above. One is that the IX system can give a lot of control to the experimenter. For example, the experimenter can control the IX density directly by changing the laser excitation power. The experimenter can control IX temperature in a cryostat since IXs have a long enough lifetime and fast enough

cooling rates to allow cooling to the lattice temperature. As stated above, the experimenter can control both the IX lifetime and energy with the applied gate voltage. The IX energy can be controlled in situ within the IX lifetime. IX mass can be controlled with a magnetic field [19]. Furthermore, excitons are optical and have transport distances larger than the diffraction limit of optical setups and can therefore have their energies and transport be studied with the use of spatially and spectrally resolved optical imaging.

1.3 Indirect exciton inner ring

Interesting exciton emission patter formation has been studied in the emission of IXs and presented in a number of works [20, 6, 21, 22, 23, 24, 25, 26, 27, 28]. Exciton pattern formation includes four main features: the excitonic inner ring, localized bright spots, the external ring, and the macroscopically ordered exciton state (MOES) within the external ring. The external ring, MOES, and localized bright spots in the exciton emission pattern are not a focus of this thesis, but are described in detail in [6].

IX transport measured in this thesis is similar to the inner ring studied in [20, 21, 22, 28]. The IX inner ring is a ring of IX photoluminescence that is observed surrounding the laser excitation spot as seen in Figure 1.3(d). The inner ring forms as follows. Excitons are created hot in the area of the hot laser excitation spot. These hot, high energy states are optically inactive (Figure 1.3(a)). Excitons cool as they travel away from the laser excitation spot via emission of phonons (Figure 1.3(b)). The cooling creates a high occupation of low-energy optically active states and a ring of exciton photo-luminescence is observed around the excitation spot (Figure 1.3(c) and Figure 1.3(d)).

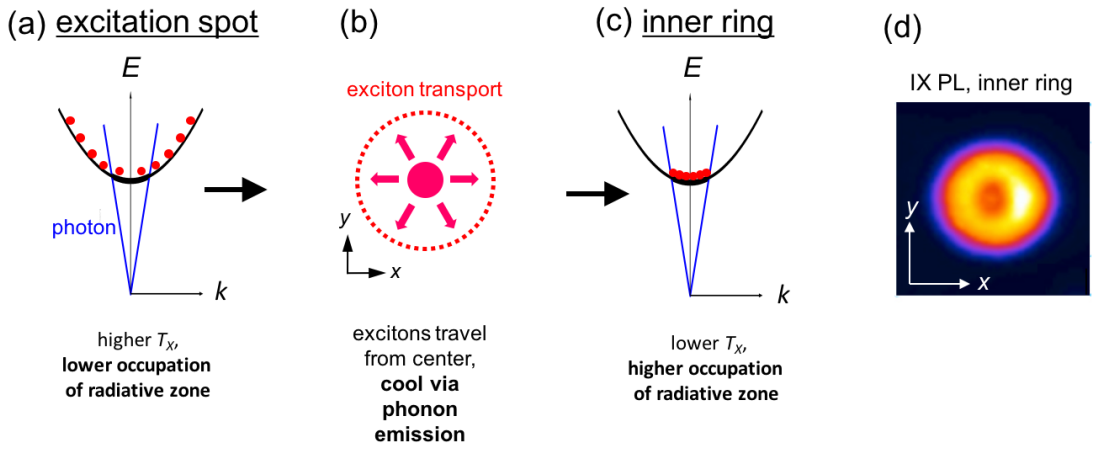

Figure 1.3: Formation of the IX inner ring. (a) In the region of the laser excitation spot, there is a high occupation of high-energy exciton states, which are not optically active. (b) As excitons travel away from the laser excitation spot, they cool via emission of phonons. (c) The cooling brings excitons to energies within the light cone, which are optically active states. IX PL consequently forms a ring shape. (d) x-y image of IX PL of the IX inner ring.

1.4 Indirect excitons as an advantageous system for the study of cold bosons in high magnetic fields

Studies of fermions in high magnetic fields have resulted in a multitude of interesting discoveries over several decades that have provided integral fundamental physics knowledge. On the other hand, studies of bosonic particles in high magnetic fields has remained limited. This limitation stems primarily from the extremely large magnetic field strengths (up to 10^6 T) that are required for cold atoms to achieve the high magnetic field regime.

As light bosons in a solid state system, excitons provide a unique opportunity to achieve the high magnetic field regime, requiring only a few Tesla which is possible to obtain in a laboratory. Furthermore, the fast cooling rates of indirect excitons allows the study of cold bosons in high magnetic fields. Theoretical background and experiments on IXs in high magnetic fields are presented in Chapter 3.

1.5 Coherence of indirect excitons

The low IX mass ($M_X = 0.22m_0$ where m_0 is the electron mass) and efficient cooling of IXs allow them to cool below the temperature of quantum degeneracy, $T_{dB} = 2\pi\hbar^2 n_X/(M_X g k_B)$. Fast cooling rates combined with long lifetimes allow IXs to cool down to the lattice temperature within their lifetime. Lattice temperatures down to $\sim$30 mK are achieved in lab with dilution refrigerators. At these temperatures, IXs are well below the temperature of quantum degeneracy where the IX separation distance approaches the IX de Broglie wavelength, $T_{dB} \sim 3$ K for the typical exciton density $n_X = 10^{10}$ cm^{-2} and spin degeneracy $g = 4$. At low temperatures, IXs have been observed to form a coherent bosonic gas with a coherence length reaching $\sim$10 μm [3]. Reference [3, 33] constitutes the first measurements of coherence of a cold exciton gas.

1.6 Excitonic devices

Due to several possible advantages, excitonic devices based on systems of IXs are being developed for possible alternative to electronic devices [4]. Excitonic devices are field effect devices that operate based on the principle of control of IX by voltage to create exciton potential energy landscapes as $U(x,y) = edF_x(x,y)$. The potential advantages of excitonic devices are listed below.

i. Excitons are optically active

As opposed to electrons which are optically inactive, excitons directly transform to photons upon radiative recombination. Optically active excitonic devices may lead to efficient coupling to optical communication.

ii. Excitons can form coherent condensates without resistance

As excitons are bosons, they can form coherent condensates in which scattering is suppressed in exciton transport. Coherent exciton condensates could provide an opportunity to create excitonic devices that operate based on currents of excitons without resistance and allow for low

switching voltage for excitonic transistors, leading to energy efficient computation.

iii. Excitonic devices scale with the exciton Bohr radius or de Broglie wavelength

The exciton Bohr radius or de Broglie wavelength is around 10 nm in typical structures. This is much shorter than photon wavelengths ($\sim$ 100 nm-1000 nm), so excitonic devices provide an opportunity to make optically active devices on sub-photon wavelength scales.

Many excitonic circuitry devices have already been realized including excitonic transistors [29, 30, 31, 32], ramps [10, 15, 34, 35], photon storage devices [36, 37], and excitonic integrated circuits [38]. These devices have been created in GaAs systems and operate at cryogenic temperatures in liquid helium cryostats, serving as proof-of-principle experiments for excitonic devices. The exciton can exist in temperatures below $k_{\mathrm{B}}T \sim E_{\mathrm{X}}$, where k_{B} is the Boltzmann constant and E_{X} is the exciton binding energy. Above this temperature the excitons may be broken apart by thermal energy. In typical GaAs/AlGaAs CQW structures, the excitons can exist up to 40 K. Some other structures involving excitons in GaAs/AlAs CQWs have achieved excitonic devices that operate up to temperatures at 100 K [31].

Large efforts are in progress to bring excitonic devices from cryogenic temperatures to room temperature to increase the feasibility of commercial excitonic devices. These efforts involve the development of IXs in structures based on 2D materials in which the exciton binding energy is high enough to allow excitons to exist at room temperature [39, 40, 41, 42].

In addition to circuitry devices, certain excitonic devices have been realized and used to perform studies of fundamental physics including exciton traps [43, 44, 45, 46, 47, 48, 49, 50, 51, 52, 53, 54], stirring potentials [55], lattices [56, 57, 49, 58, 59, 60], and conveyers [61]. Chapters 4 through 6 present developments in excitonic circuitry devices and devices for fundamental physics studies of mesoscopic physics of IXs.

1.7 Outline of the dissertation

This dissertation includes studies of fundamental physics of IXs in high magnetic fields as well as developments in the field of excitonic devices. Chapter 2 describes the primary experimental method used, optical spectroscopy, in addition to detailing the nano-fabrication process for excitonic devices.

Chapter 3 consists of a study of IXs in high magnetic fields which involved time-resolved optical imaging. A theoretical overview is presented along with experimental data on kinetics of IXs in high magnetic fields.

Chapter 4 through 6 are mainly focused on the development of excitonic devices. Chapter 4 presents a new perforated electrode method for the creation of excitonic devices. Chapter 5 includes the first realization and characterization of an excitonic split-gate device. Chapter 6 presents IX studies in a wide single quantum well structure, which provides a novel platform for excitonic devices with high IX mobility.

Chapter 2

Experimental Methods

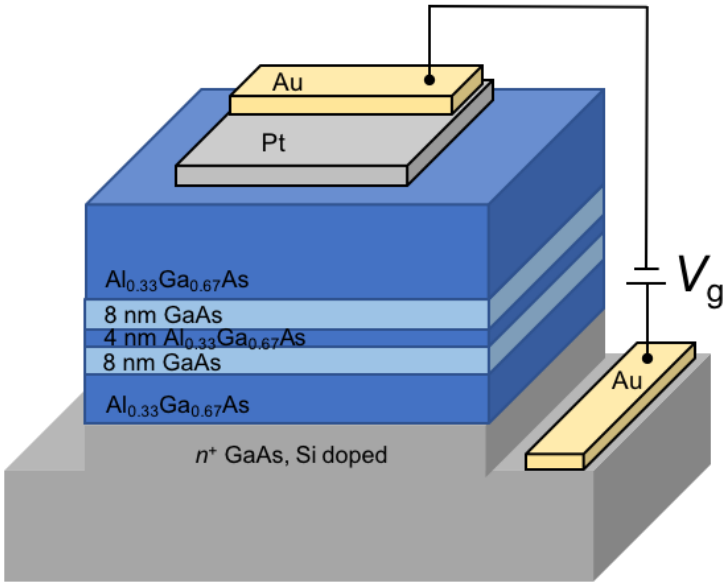

Figure 2.1: A typical GaAs coupled quantum well device. The *n*+ GaAs Si doped bottom layer is bonded with gold and serves as the homogeneous bottom electrode. Top electrodes are patterned with Pt and electrically contacted with gold. Typical structures include two 8 nm GaAs quantum wells which are separated by a 4 nm AlGaAs barrier layer.

2.1 Coupled quantum well layered semiconductor heterostructures

The work presented in this thesis studies IXs in GaAs/AlGaAs CQW heterostructures grown by molecular beam epitaxy. Typical sample structures, as show in Figure 2.1, consist of a Si doped n^+ GaAs back gate with n_{Si} around $\sim 10^{18}$ cm^{-3}, which serves as a homogeneous bottom ground electrode. A set of GaAs coupled quantum wells are grown inside a barrier material of $Al_{0.33}Ga_{0.67}As$. Typical QW widths are 8 nm with a barrier between of 4 nm. CQW dimensions are chosen as such to optimize IX binding energy, lifetime, and large energy shift by applied voltage.

The spacing between the CQWs and the n^+ GaAs back gate is typically 100 or 200 nm, and the total thickness of the $Al_{0.33}Ga_{0.67}As$ barrier is 1 μm. The WSQW is positioned closer to the homogeneous bottom electrode to suppress the fringing in-plane electric field F_{r} in excitonic devices [49]. Otherwise, a high F_{r} could lead to IX dissociation [56].

The CQWs are positioned closer to the homogeneous back gate to reduce in-plane field from fringing field effects that may cause IX dissociation .

2.2 Optical spectroscopy of indirect exciton photoluminescence

Optical spectroscopy is employed to study IX behavior and to characterize IX devices. A typical experimental setup is shown in Figure 2.2. Measurements are performed as follows. IXs are generated with laser excitation. In this thesis, a HeNe laser at 633 nm focused to a point-like excitation spot is primarily used. When IXs recombine and emit a photon – IX photoluminescence (PL), the IX PL is focused to a spectrometer and imaged with a nitrogen cooled charge-coupled device (CCD) camera. In this way, spatially and spectrally resolved images are captured. All measurements are performed at cryogenic temperatures which are achieved in liquid helium

cryostats and a dilution refrigerator with windows to perform optical measurements.

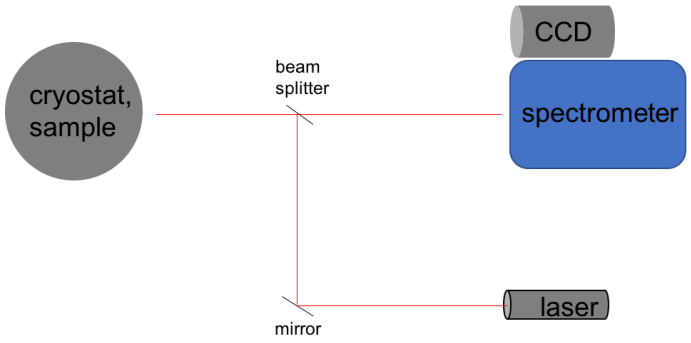

Figure 2.2: Schematic of optical spectroscopy setup. An optical liquid helium cryostat houses the sample. Excitons are generated with laser excitation. Exciton PL is captured with a liquid nitrogen cooled CCD that is coupled to a spectrometer.

Additionally, time-resolved imaging is also used to study IX kinetics, in which the CCD is augmented with an intensifier and the intensified CCD (ICCD) camera is used to take short, few ns images over time to observe evolution of IX behavior. Time-resolved imaging is explained in more detail and used for measurements in Chapter 3.

2.3 Nano-fabrication of excitonic devices

The CQW structures studied in this thesis require a voltage applied perpendicular to the QW planes to achieve the indirect regime as discussed in Section 1.1. As seen in Figure 2.1, the n^+ GaAs layer serves as a homogeneous bottom electrode. This layer is electrically contacted by etching about 100 - 200 nm into the layer and depositing a few hundred nm layer of gold with electron beam evaporation, which is then wire bonded. A thin layer of $\sim$ 20 nm of Ti is added under the gold layer to help with adhesion of the gold to the sample.

The top electrodes are created by depositing a thin layer of 7 nm of Pt with electron beam evaporation. A layer of 2 nm of Ti is again deposited below the Pt layer to help with the Pt adhesion. A thin layer of Pt is chosen for the electrode due to its high conductivity to create a

good electrode, and high transparency to allow for IX PL to pass through. Using these thin layers of Pt can also be advantageous for creating devices with small feature sizes.

Simple, large electrodes that generate flat IX potentials can be used to simply achieve IX regime and study basic IX transport as in Chapter 3 and 6. However, more specially engineered excitonic devices which create more complicated potentials to control IX transport in a specific way require careful patterning of electrodes. For these devices, IX potential energy profiles from certain electrode geometries are first designed and simulated with COMSOL. These specialized devices require electron beam lithography to achieve small electrode features and spacings. Chapters 4 and 5 explain in more detail the design process for the excitonic ramp device and the excitonic split-gate device.

Chapter 3

Kinetics of Indirect Excitons in High Magnetic Fields

3.1 Introduction to high magnetic field regime for indirect excitons

The study of fermions in high magnetic fields have resulted in remarkable observations such as the integer and fractional quantum hall effects [104]. Such rich phenomena in fermionic systems inspire similar measurements to be performed on bosonic systems. However, the study of bosons in high magnetic fields has been limited due to the magnitude of magnetic field required. The high magnetic field regime for bosons is defined as the regime where the cyclotron energy is comparable to the binding energy. For atoms, this regime would require magnetic fields on the order of 10^6 T, so studies of atoms in magnetic fields have been limited to synthetic fields [62, 63, 64, 65].

The IX system provides a unique opportunity to study cold bosons in the high magnetic field regime, because the high magnetic field regime for IXs require magnetic fields on the order of a few Tesla, which is achievable in a laboratory. This is due to the IX small effective mass,

which gives a large cyclotron energy, and small binding energy (IX has cyclotron energy $\hbar\omega_c = \hbar eB/(\mu c)$ and binding energy $E_b \sim (\mu e^4)/(2\varepsilon^4\hbar^2)$).

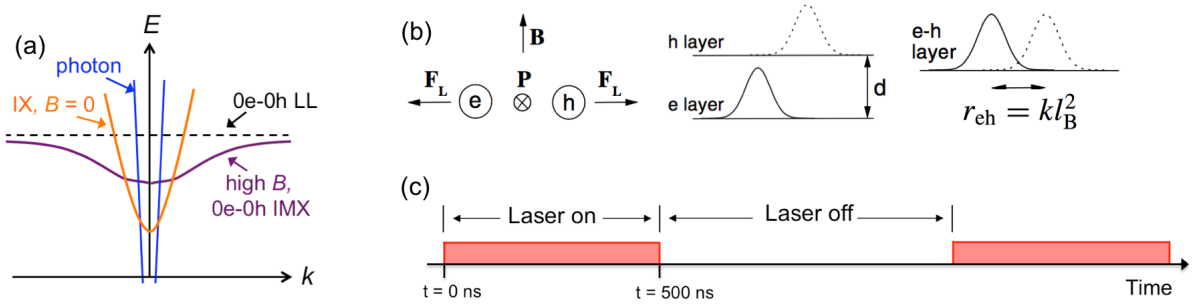

Figure 3.1: (a) IX in zero magnetic field has simple quadratic dispersion relation (orange curve). IMX dispersion curve is modified in high magnetic field (purple curve). (b) In high magnetic field, coupling occurs between electron and hole separation distance and IX center of mass momentum. (c) Pulse profile used in time-resolved imaging experiment.

Excitons in a high magnetic field exhibit behavior different than excitons in zero magnetic field [66, 67, 68, 73, 69, 72]. Firstly, excitons in zero magnetic field are hydrogen-like particles, whereas magnetoexciton (MX) wavefunctions are composed of an electron and a hole each in a Landau level (LL) state. Figure 3.1(a) shows the exciton and MX dispersion including a 1s exciton dispersion at $B = 0$ (orange curve) and the corresponding 0e-0h IMX dispersion (purple curve) (0e-0h indicates an MX composed of an electron and hole both in the zeroth LL state). The filling of these LL states may also be controlled via laser excitation power, which is another advantage of the IX system for the study of cold boson in high magnetic field. As magnetic field decreases, N_e - N_h MX states transform to (N + 1)s exciton states, where N + 1 is the principal quantum number of the exciton relative motion.

Secondly, the exciton mass in zero magnetic field is simply the sum of the mass of the electron and hole. In contrast, the mass of an MX becomes dependent on the magnetic field, and in the high magnetic field limit, becomes approximately independent of the mass of the electron and the hole. The magnetic field dependence of the MX mass stems from a coupling that occurs between the IMX center of mass momentum and the MX dipole moment: $r_{eh} = kl_B^2$ where l_B =

$\sqrt{(\hbar c/eB)}$ is the magnetic length. At the basis of this coupling is the fact that the electron and a hole of a MX are forced to travel with the same velocity and produce on each other a Coulomb force that is balanced by the Lorentz force. Figure 3.1(b) shows graphically the coupling. The coupling between r_{eh} and k allows the MX dispersion $E(k)$ to be calculated from the Coulomb potential between the electron and the hole as a function of r_{eh}.

The MX dispersion is parabolic at small k and can therefore be described with an effective MX mass which is dependent on the strength of the magnetic field. At high $k >> 1/l_B$, the separation between the electron and hole becomes large due to the coupling explained above, and therefore the Coulomb interaction between them vanishes, and the MX energy tends toward the sum of the electron and hole LL energies [66, 67, 68, 73]. The MX mass and MX binding energy are generally both dependent on magnetic field and increase with B [66, 67, 68, 73, 70].

The above properties apply to direct MXs (DMXs) and indirect magnetoexcitons (IMXs), but DMXs and IMXs experience other differences. Due to the separation d between the e and h layers, IMX energies are lower by edF_z (where F_z is electric field in z due to applied voltage) and increase faster with B[71, 74, 75, 76, 77, 78, 79], IMX binding energies are smaller [73, 74, 79, 19, 80], and IMX effective masses increase faster with B [73, 79, 19, 80]. At voltages where DMX and IMX are close in energy, a nonmonotonic dependence on B can be observed [80].

The experimental work presented in this chapter uses optical spectroscopy to study PL emission of IMXs. Free two-dimensional IMXs can recombine radiatively when the following conditions are met: (i) Their momentum k is inside the intersection between their dispersion surface and the photon cone (Figure 3.1(a)), called the radiative zone [8, 82, 81, 83]; in GaAs structures this gives $k = k_0 \leq E_g\sqrt{\varepsilon}/(\hbar\omega_c) \sim 2.7 * 10^5$ cm^{-1} where ε is the dielectric constant and E_g is the semiconductor band gap. (ii) $N_e = N_h$ where N_e and N_h are the LL numbers of the electron and hole. (iii) The spin projection in the z direction J_z = +/- 1. Free IMXs with $k > k_0$, $N_e \neq N_h$, or J_z = +/- 2 are dark.

Earlier work on IMXs involved studies of IMX energy [71, 74, 75, 76, 77, 78], dispersion relations [73, 79, 19, 80], and spin states [85, 86]. Two-dimensional neutral exciton and deexcitons were studied in high magnetic fields in dense e-h plasmas [84, 87], but these studies were performed in single QW structures which did not allow the achievement of low IMX temperatures and limited exciton transport.

This work focuses on IMX transport. Earlier work which involved imaging of the IMX emission cloud in cw experiments showed evidence for long-range transport of IMXs composed of electrons and holes in the lowest LLs [88]. The work presented in this chapter reports on the first direct measurement of IMX transport by utilizing time-resolved measurements to observe IMX cloud expansion.

3.2 Experimental method

For this experiment, a typical GaAs CQW structure grown by molecular beam epitaxy was employed to study IXs. The structure geometry includes 8 nm GaAs QWs separated by a 4 nm $Al_{0.33}Ga_{0.67}As$ barrier, surrounded by 200 nm $Al_{0.33}Ga_{0.67}As$ layers. This sample has two doped n^+ GaAs layers surrounding the QW region, which are Si doped GaAs with $n_{Si} = 5 * 10^{17}$ cm^{-3}. These n^+ layers serve as the gates of the semiconductor structure. For all data, the indirect regime is achieved by applying voltage $V_g = 1.4$ V across the n^+ layers.

Time-resolved optical imaging was performed using a pulsed semiconductor laser excitation with a 658 nm wavelength and pulse duration of $\tau_{width} = 500$ ns, pulse period of $\tau_{pulse} = 1.3$ μs, with an edge sharpness of 1 ns as shown in Figure 3.1(c). The rectangular-shaped pulses were achieved by use of a pulse generator driving the semiconductor laser. This pulse period and duty cycle were chosen to allow the IMX PL image to reach an equilibrium by the end of the laser excitation and to allow full decay between laser pulses.

The images were taken with a CCD coupled to a PicoStar HR TauTec time-gated intensifier

are were integrated over 4 ns windows (δt = 4 ns) and taken for several delay times t after the onset of the laser pulse, defined such that a delay time t corresponds to an image taken during time $t = t$ - δt to t.

To perform the optical imaging measurements in high magnetic field, an optical dilution refrigerator with a superconducting magnet was used. All measurements were performed at T_{bath} = 1.5 K with applied magnetic fields up to 10 T oriented perpendicular to the CQW plane. The spectrally and time-resolved imaging directly measures the evolution of the IX PL intensity and energy as a function of delay time t, showing the expansion of the IMX cloud over time due to IMX transport.

3.3 Experimental results and discussion

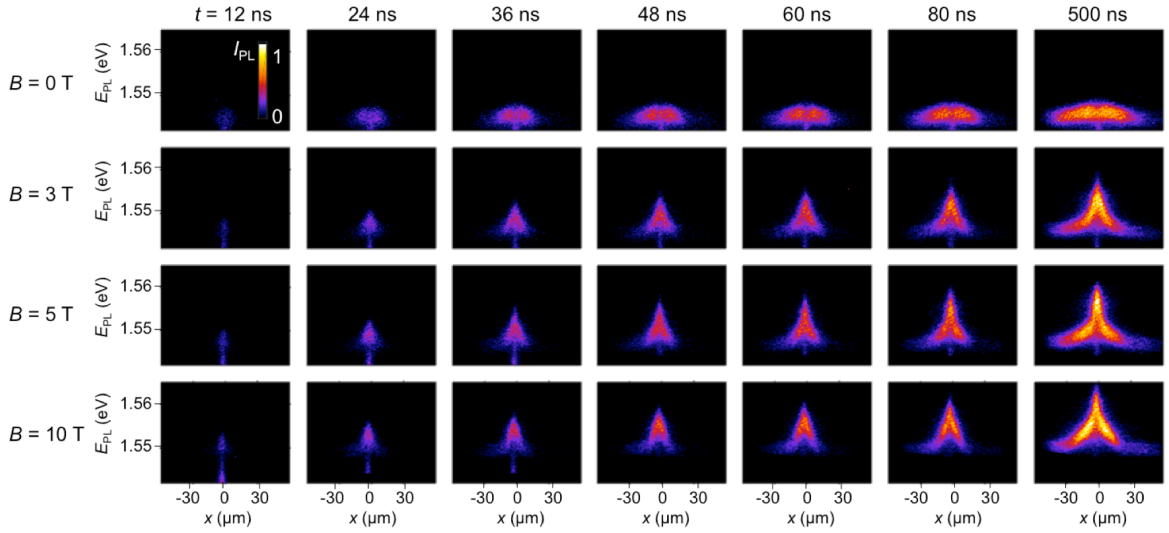

Figure 3.2: x-energy time-resolved images of IMX PL for B = 0 to 10 T for several delay times. The laser excitation spot is centered around x = 0. P_{ex} = 670 μW.

Figure 3.2 shows a subset of the IMX PL time-resolved imaging data. The images are resolved in space, energy, and time. Each row is data taken at a different magnetic field strength, listed on the left of each row. Expansion of the IMX cloud in the x-axis with time is due to

IMX transport. Growth of the IMX cloud in the y-axis with time represents an IMX energy shift. The laser excitation was focused to a $R_0 = 4.5$ μm half width at half maximum (HWHM) spot, centered at $x = 0$.

Analysis of the data set revealed several novel observations on the kinetics of IMXs, which are explained individually in detail below.

i. IMX mass increase and diffusion coefficient measurement

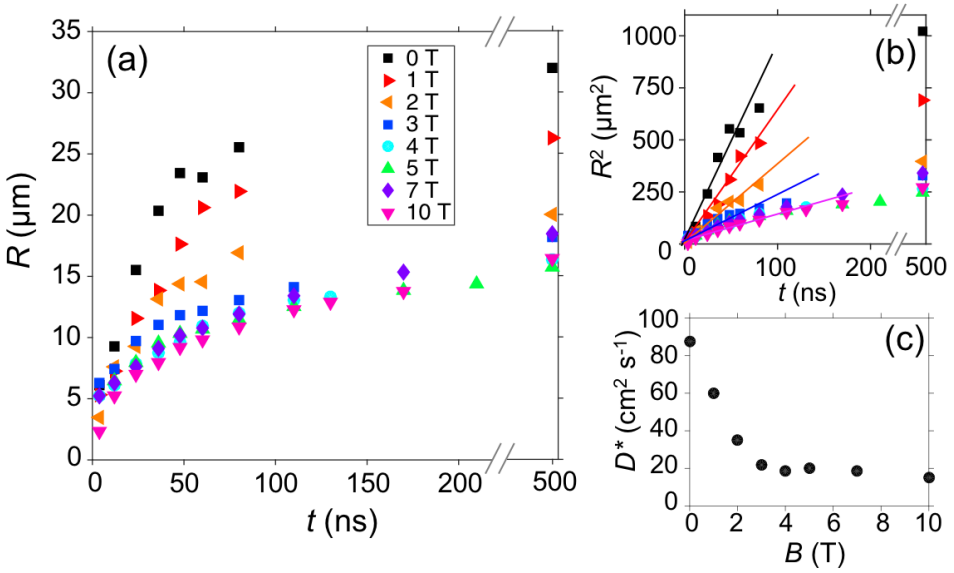

Figure 3.3: (a) Radius of IMX cloud vs time delay after laser termination for several magnetic field strengths. (b) Radius squared vs. time delay for IMX cloud. Linear fits allow for extraction of IMX diffusion coefficient. (c) IMX diffusion coefficient vs. B.

Figure 3.3(a) shows the IMX transport radius as a function of delay time during the laser pulse for several magnetic field strengths. The slope of R vs. t decreases with increasing magnetic field; there is slower and shorter transport at higher magnetic fields. This is due to the increase of IMX mass with magnetic field as described in section 3.1. The IMX mass increase affects IMX diffusion and drift as both the exciton diffusion coefficient D and the exciton mobility μ_X are inversely proportional to the mass [9], and thereby causes a reduction in transport.

In addition to allowing the direct measurement of transport, time-resolved imaging also allows for an experimental extraction of the diffusion coefficient, D^*. By fitting to the slope

of $R^2 \sim R_0^2 + D^* t$ as plotted in Figure 3.3(b), one can extract an experimental estimate of the effective IX diffusion coefficient D^*, which encapsulates both D and μ_X. A full expression for D^* is presented in the theory below, Section 3.4. Figure 3.3(c) shows the experimentally measured D^* as a function of magnetic field. D^* decreases with increasing magnetic field due to the IMX mass increase.

ii. Evolution of IMX energy with time

The time-dependence of the IMX PL energy was also studied. Figure 3.4(a) and (b) show the IMX average PL energy as represented by the first moment $M_1(x) = \int EI(x,E)dE / \int I(x,E)dE$ as a function of delay time t for B = 5 T. Two effects are observed: the IMX PL blue shifts during the laser pulse after the laser pulse onset, and the IMX PL red shifts after the termination of the laser pulse. It was also observed that the magnitude of the energy shift is dependent on magnetic field as seen in Figure 3.4(c), and the shift is stronger for higher magnetic field. Here the energy shift is calculated as $M_1(t)$ - $M_1(t = 12ns)$ at x = 0. The energy shift is described in terms of increased IMX mass as follows. Transport away from the IMX generation site is suppressed at higher magnetic fields due to the IMX mass increase, which reduces IMX drift and diffusion. The transport suppression leads to an increased IMX density near their generation site in the region of the laser excitation spot. As IXs are oriented dipoles, they have repulsive interactions. So, as the IMX density increases due to the transport suppression, the IMX repulsive interactions lead to a blue shift over time. Conversely, as the IMX density begins to decay after laser termination, the IMX energy red shifts. Figure 3.4(d) characterizes this effect and shows that the energy shift is stronger for shorter transport radii.

iii. Increase of IMX transport distance and energy shift with laser excitation power

A laser excitation power dependence on the IMX kinetics study was performed. Figure 3.5(a) shows the evolution of the radius of the IMX cloud due to IMX transport for two different laser excitation powers. Long-range IMX transport was observed at the higher laser excitation power of P_{ex} = 670 μW, while the IMX cloud profile remained approximately the size of the

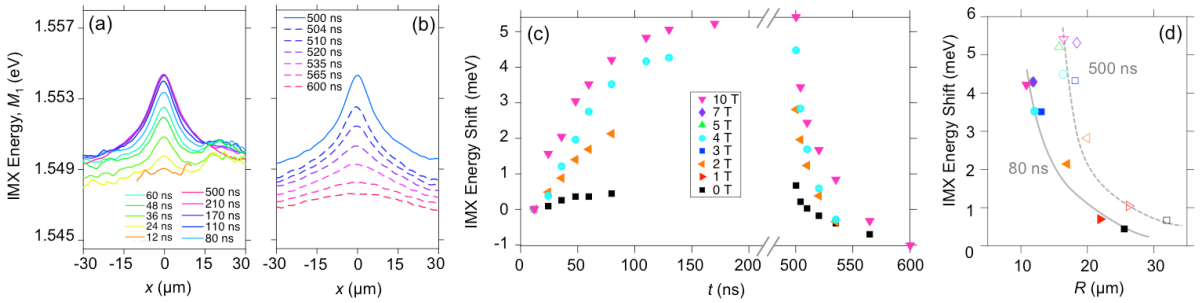

Figure 3.4: IMX energy represented as the first moment of IMX PL $M_1(x)$ for different delay times (a) during the laser pulse and (b) after the laser pulse termination. All data at B = 5 T. (c) IMX energy shift $M_1(t)$ - $M_1(t = 12ns)$ at x = 0. (d) IMX transport radius R vs IMX energy shift at x = 0 for several magnetic field strengths at two delays: t = 80 ns (filled markers) and t = 500 ns (open markers). T_{bath} = 1.5 K and average P_{ex} = 670 μW for all data.

laser excitation profile for the low laser excitation power of 25 μW; essentially no transport was observed for the lower laser excitation power. The discrepancy in transport distance between the low and high laser excitation power can be explained in terms of disorder screening by IXs. At higher laser excitation power, which corresponds to higher IX density, the IXs effectively screen out disorder in the QWs and allow long-range transport to occur. In contrast, at lower laser excitation powers which correspond to lower IX density, the IXs may become localized in the disorder potential and transport is not observed.

Additionally, in Figure 3.5(b), a stronger IMX energy shift is observed for the higher laser excitation power. This is due to stronger repulsive interactions present in higher densities of IXs.

iv. IMX lifetime increase

The decay of the IMX signal after the laser pulse termination is studied and presented in Figure 3.6. The lifetime of the IMX can be measured with the decay of the total IMX intensity over time. Figure 3.6(b) shows total IMX intensity integrated over space and energy as a function of time after laser termination. A fit to the decay curve gives IMX lifetime. As shown in Figure 3.6(c), the IMX lifetime was observed to increase with increasing magnetic field. The IMX lifetime increase results from the dispersion flattening (as described in Section 3.1) which reduces the energy width of the radiative zone and therefore gives an increased IMX lifetime.

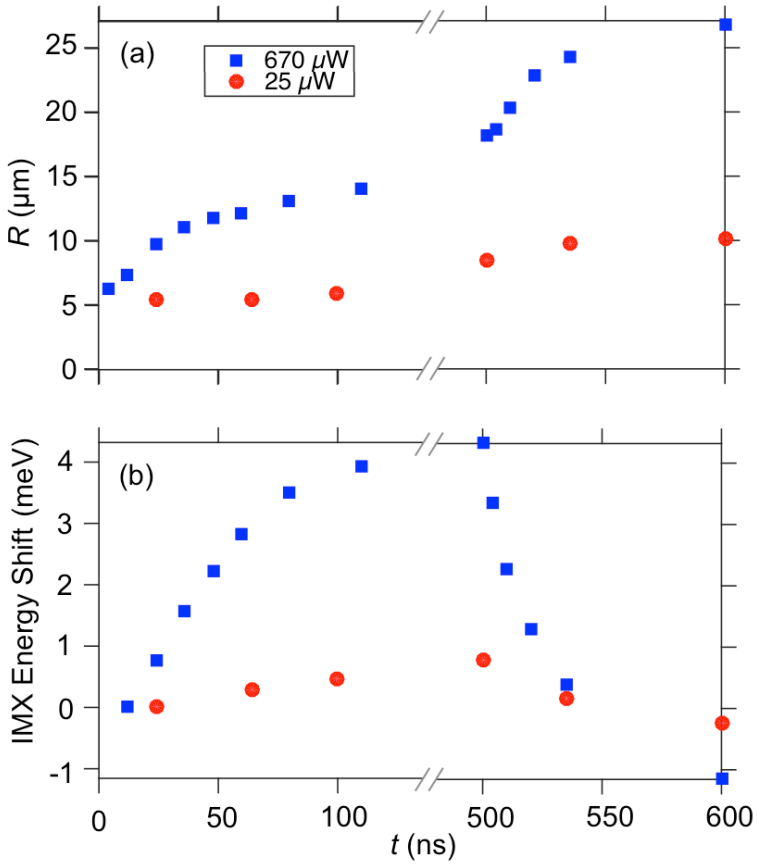

Figure 3.5: (a) Radius of IMX cloud vs time delay for two laser excitation powers P_{ex} = 670 μW (blue squares) and 25 μW (red circles). (b) IMX energy shift at $x = 0$ vs time delay t. T_{bath} = 1.5 K and B = 3 T for all data.

3.4 Simulations

The IMX kinetics in high magnetic field presented here were simulated with a model based on IX transport and thermalization. Two coupled equations for the IMX density n and temperature T were solved,

$$\frac{\partial n}{\partial t} = \nabla\left[D\nabla n + \mu_x n \nabla(u_0 n)\right] + \Lambda - \frac{n}{\tau}, \tag{3.1}$$

$$\frac{\partial T}{\partial t} = S_{\text{pump}} - S_{\text{phonon}}\,. \tag{3.2}$$

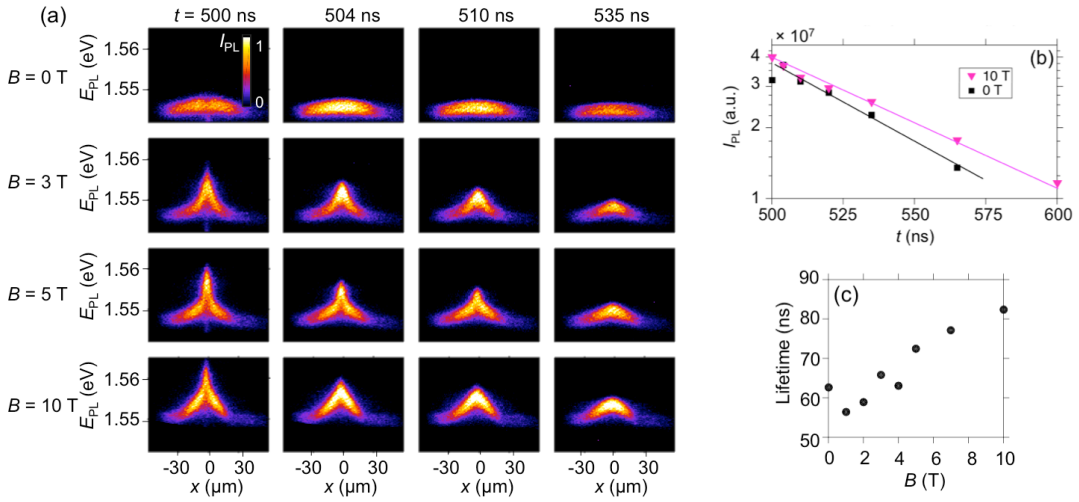

Figure 3.6: (a) x-energy time-resolved images of IMX PL for $B = 0$ to 10 T for several delay times after the laser pulse termination. (b) Total spectrally and spatially integrated IMX PL intensity for $B = 0$ and 10 T for several delay times after laser termination. (c) IMX lifetime as a function of magnetic field.

Here, ∇ is the 2D nabla operator using cylindrical symmetry. The first term in square brackets in equation (3.1) describes IMX diffusion. The diffusion coefficient $D(n,T,M)$ is inversely proportional to the IMX effective mass $M(B)$ and describes the magnetic field induced reduction in IMX transport. D also accounts for the screening of the random QW disorder potential by IMXs [9, 21, 22]. The mobility μ_X is given by $\mu_X = D(e^{T_0/T} - 1)/(k_B T_0)$ where $T_0 = \pi\hbar^2 n/(2M(B)k_B)$ is the quantum degeneracy temperature. It can be seen from equation 3.1, that the experimentally estimated diffusion coefficient, D^*, as discussed above in Section 3.3 is represented as $D^* \approx D + \mu_X n u_0$.

The second term in equation (3.1) describes IMX drift which originates from the repulsive dipolar interactions and is approximated by $u_0 = 4\pi e^2 d/\varepsilon$ [22].

The IMX generation rate Λ has a Gaussian profile approximately matching that of the laser excitation spot. τ is the IMX optical lifetime. Equation (3.2) describes thermalization of excitons: heating of excitons by non-resonant photo-excitation, $S_{\text{pump}}(T_0,T)$ and cooling via interaction with bulk longitudinal acoustic phonons, $S_{\text{phonon}}(T_0,T)$. The emission intensity is

extracted from n/τ. Expressions for D, S_{pump}, S_{phonon} and τ can be found in [22].

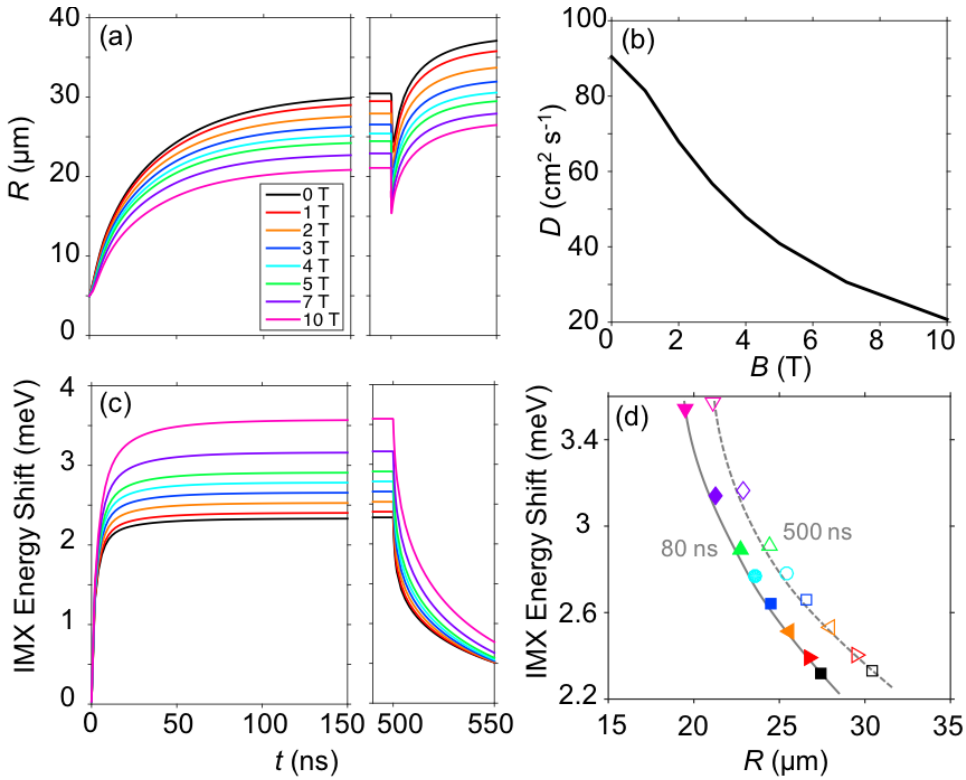

Figure 3.7: Results of simulations. (a) Simulated IMX transport distance R vs. delay time t. (b) Spatially averaged diffusion coefficient D vs. B for delay time $t = 10$ ns. (c) Calculated IMX energy shift at $x = 0$ vs. t. (d) IMX energy shift at $x = 0$ vs. R for $t = 80$ ns (filled markers) and $t = 500$ ns (open markers).

The magnetic field dependence plays a role in the model in a few ways. Equations (3.1-3.2) are affected by magnetic field via D and T_0 since both depend on $M(B)$. Furthermore, τ is given by the single $k = 0$ IMX lifetime $\tau_r(B)$ divided by the fraction of IMXs that are inside the radiative zone. The radiative zone is the region in momentum space contained within the intersection between the photon and exciton dispersion surfaces, the latter being a function of $M(B)$. The magnetic field can affect the exciton lifetime in two ways: (i) Increasing $M(B)$ will decrease of the energy width of the radiative zone which lowers its occupation and enhances τ. (ii) the magnetic field shrinks the in-plane Bohr radius, increasing the probability of electron-hole recombination and thus decreasing τ. $M(B)$ and $\tau_r(B)$ were determined in Refs. [89, 80].

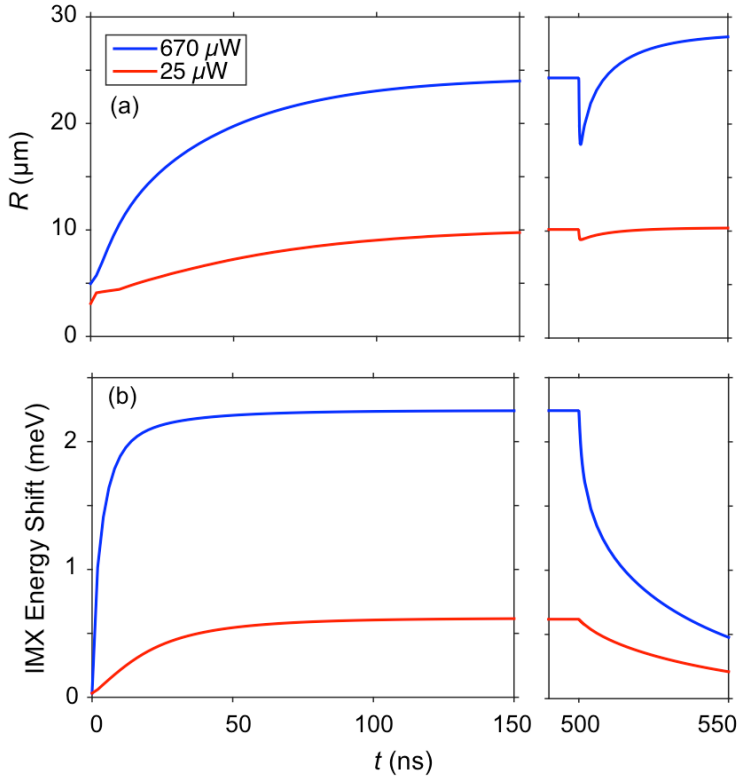

Figure 3.8: Results of simulations. (a) Simulated IMX transport radius vs. delay time t for two laser excitation powers P_{ex} = 670 μW (blue squares) and 25 μW. (b) Simulated IMX energy shift at x = 0 vs delay time t.

Figure 3.7 summarizes some results of the simulations. Figure 3.7(a) shows the calculated IMX transport distance R vs. delay time t for several magnetic field strengths. The calculations show the transport radius to decrease with increasing magnetic field, qualitatively consistent with the experimental data of Figure 3.3(a). A diffusion coefficient may be extracted from the simulated data and results in a diffusion coefficient that decreases with increasing B, in agreement with the experimental result shown in Figure 3.3(c).

The calculated IMX energy shift vs. delay time is plotted in Figure 3.7(c) and shows stronger IMX energy shift for higher magnetic fields. This is in qualitative agreement with the data presented in Figure 3.4(c). Additionally, the decline in IMX energy shift with increasing radius appears in the simulations; compare Figure 3.4(d) and Figure 3.7(d).

A qualitative discrepancy between the experimental and calculated data is observed directly after the termination of the laser excitation: a "kink" is observed in the R vs. t plots in the calculated data (Figure 3.7(a) and Figure 3.8(a)). This can be explained in terms of IX heating and cooling. As described in Section 1.3, IX PL intensity is suppressed in the excitation spot region (IX inner ring) during the excitation pulse due to the laser-induced heating of IXs resulting in a lowering of the radiative zone occupation [20, 21, 22, 28, 88]. After the excitation pulse termination, IXs cool down, and the IX PL intensity increases at the excitation spot region a few ns after the excitation pulse ends [22]. This results in the apparent reduction in R, or "kink", as seen in Figure 3.7(a) and Figure 3.8(a). This kink is not observed in the experiment within the experimental resolution.

Furthermore, upon looking closer at the IMX kinetics after the laser pulse termination, an enhancement of R after the pulse termination is observed in both the simulations (Figure 3.7(a) and Figure 3.8(a)) and the experiment (compare Figure 3.5(a) to Figure 3.8(a)). This enhancement of the IMX transport distance is consistent with a better screening of the QW disorder potential by colder IMXs.

Figure 3.8(a) shows the calculated power dependence of the IMX transport radius vs. delay time t. Long-range transport is observed only for the higher laser excitation power. This is in agreement with the experimental result shown in Figure 3.5(a) and as explained above is due to effective disorder screening of IXs at higher IX density. Figure 3.8(b) shows the calculated IMX energy shift as a function of delay time for the two laser excitation powers. Again, in agreement with the experimental data shown in Figure 3.5(b), a higher energy shift is observed at the higher IMX density (higher laser excitation power), stemming from the stronger repulsive interactions present at higher IX density.

3.5 Acknowledgements

The text of chapter 3, in part, is a reprint of the material as it appears in C. J. Dorow, M. W. Hasling, E. V. Calman, L. V. Butov, J. Wilkes, K. L. Campman, and A. C. Gossard, Spatially resolved and time-resolved imaging of transport of indirect excitons in high magnetic fields. *Physical Review B* 95, 235308 (2017), ©2017 American Physical Society, where the dissertation author was the first author. The co-authors in these publications directed, supervised, and co-worked on the research which forms the basis of this chapter.

Chapter 4

Perforated Electrode Method for Excitonic Devices

The goal of the work presented in this chapter was to develop a method to enable creation of excitonic devices with virtually any potential energy landscape and geometry that have low power consumption. Earlier work proposed to use specially designed single electrodes as devices to eliminate energy loss that occurs in devices using multiple electrodes due to leakage current between neighboring electrodes held at different voltages [91]. The work presented in this chapter constitutes the first proof-of-principle experiment for the method for creating excitonic devices proposed in Reference [91]. The physical basis behind the design of such single electrode devices is described in section 4.1.

4.1 Introduction to indirect exciton control by electrode density

Several IX devices have been made by creating potential landscapes by laterally modulated voltage $V(x,y)$ to shift the IX energy with the applied electric field by edF_z. Devices generated in

such a way often involve the positioning of separate electrodes near to each other, on the order of 100 nm spacing, that are held at different voltages to achieve the desired potential energy profile. This can be problematic for device efficiency because neighboring electrodes held at a voltage difference can have current leakage between them, which has two negative consequences: (i) more power is required to operate the device and (ii) the leakage current will inject some heat into the IX system which is not ideal for studies of ultra cold Bose gases of IXs. Some earlier device work using laterally modulated voltage includes references [4].

An alternative to laterally modulating voltage was proposed in [91], which involves modulating the surface area density of a single electrode at a constant voltage to control IX transport. Simulations of electrode density modulation are shown in Figure 4.1 and Figure 4.2. The principle of the electrode density method for creating IX devices is based on the fringing electric field effect. Due to fringing electric fields, the normal component of the applied electric field will be reduced near electrode edges; thin electrode strips will apply a weaker electric field than large electrodes, even if they are held at the same voltage. Figure 4.1(b) shows that increasing electrode density leads to an increased applied normal component of the electric field which, in turn, leads to a lower exciton energy.

This effect can be exploited to design complex potential energy landscapes which can be fabricated with just a single electrode and constant voltage, such as the elevated ramp simulated in Figure 4.2. Using a single electrode in this way eliminates leakage currents between neighboring electrodes and therefore leads to energy efficient low power devices and low temperature fundamental studies of IXs.

The physical realization and testing of this electrode density method was first performed on a shaped ramp electrode which increased in width going down the ramp [35]. This ramp successfully acted as a diode for IXs, however the simple "shaping" of the electrode width gave some limitations of possible ramp sizes. The limit of the shaped ramp size occurs because as the ramp widens (which could allow for the control of larger IX fluxes), the center of the ramp

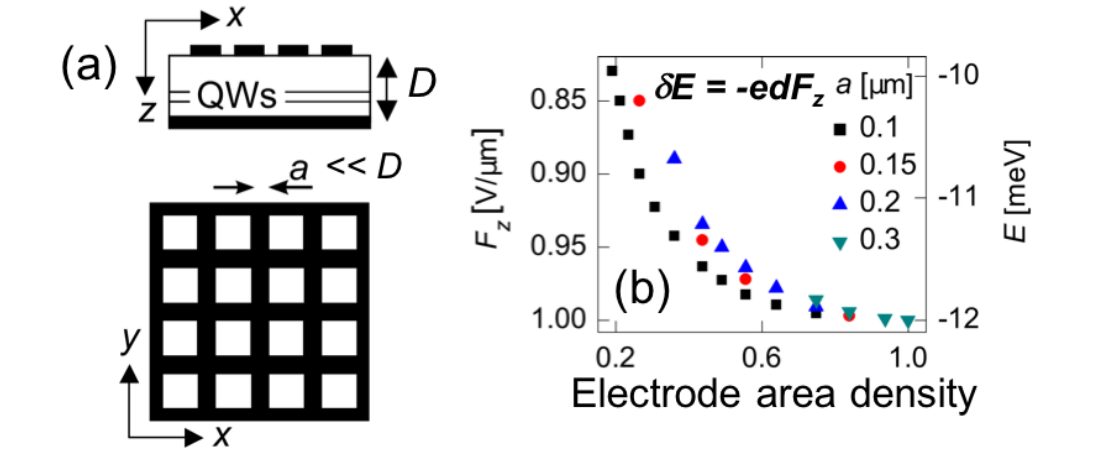

Figure 4.1: (a) Side and top view of simulated electrode pattern with varying electrode density. Electrode density is varied by changing D and a. (b) Simulated normal component of applied electric field, F_z, and IX energy shift, E, versus electrode surface area density for four different sizes of a. Increasing electrode density results in a larger IX energy shift. [91]

becomes farther from the electrode edges where the fringing field is present, and the center of the ramp therefore approaches a flat potential. To overcome this geometrical limitation, a ramp using a perforated electrode of constant width was realized, which is the subject of the chapter.

4.2 Perforated electrode ramp device fabrication

The perforated electrode is designed such that the ramp electrode has small perforations that decrease in size going down the ramp (schematic presented in Figure 4.3(a)). This achieves an electrode density gradient, resulting in a ramp potential that decreases IX energy toward the bottom of the ramp (Figure 4.3(b) and (d)).

The perforated ramp was fabricated on a CQW structure with an n^+ GaAs layer with n_{Si} = 10^{18} cm^{-3} which served as a homogeneous ground plane electrode. Two 8 nm GaAs QWs with a 4 nm $Al_{0.33}Ga_{0.67}As$ barrier are positioned 100 nm above the n^+ GaAs layer inside an undoped 1 μm thick $Al_{0.33}Ga_{0.67}As$ layer. The top semitransparent electrode was fabricated by depositing 2 nm Ti, 7 nm Pt, and 2 nm Au with electron beam evaporation. An SEM image of the fabricated

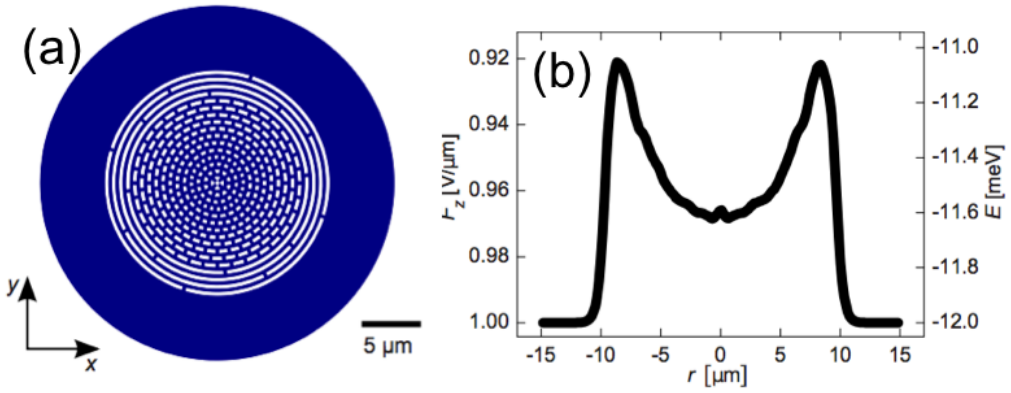

Figure 4.2: (a) A schematic of a single perforated electrode that results in an elevated trap potential. The elevated trap potential is plotted in (b). [91]

device is shown in Figure 4.3(c).

4.3 Proof-of-principle experiment

The proof-of-principle demonstration of the perforated electrode method for developing excitonic devices was performed by characterizing the ramp device with IX PL imaging. IXs were photo-generated by a 633 nm HeNe laser focused to a spot with full width half maximum 6 μm. Figure 4.4 summarizes the ramp characterization. Figure 4.4(a) and (b) show IX PL emission in a flat channel, which is simply an electrode without perforations at a constant width of 5 μm. IX transport is observed to be symmetric around the laser excitation spot, which is similar to the IX inner ring described in section 1.3. In contrast, IXs excited at the top of the ramp potential are successfully directed down the ramp (Figure 4.4(c-d)). An estimated correction for the IX PL with accounting for the semi-transparency of the device electrode is show as a dashed line in Figure 4.4(c).

The average transport distance down the ramp is calculated as $M_1 = \int xI(x)dx / \int I(x)dx$, and presented in Figure 4.3(e) as a function of laser excitation power. It was observed that the IX

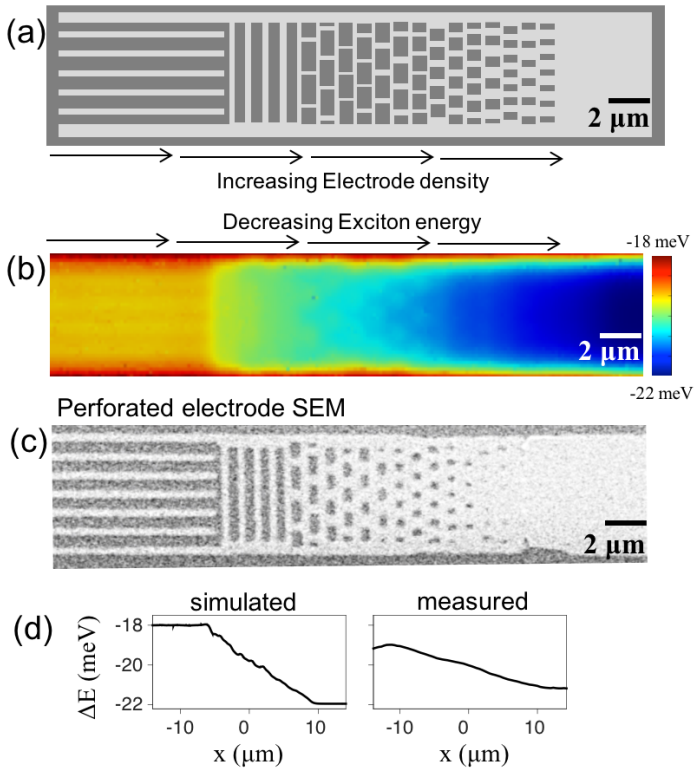

Figure 4.3: (a) Schematic of the perforated ramp electrode. The light gray is the platinum electrode. The electrode density increases going down the ramp. (b) The resulting simulated perforated ramp potential energy profile. The IX energy shift to lower energy is stronger going down the ramp, corresponding to higher electrode density. (c) An SEM image of the fabricated perforated ramp electrode. (d) The simulated and measured energy profile of the ramp device measured at the center of the width of the ramp.

transport distance down the ramp increases with increasing laser excitation power. This effect occurs due to disorder screening. As IX density increases, the disorder of the CQW structure is better screened due to repulsive IX interactions which facilitate disorder screening. Due to the efficient disorder screening at higher IX densities, the IX transport down the ramp increases at higher laser excitation powers.

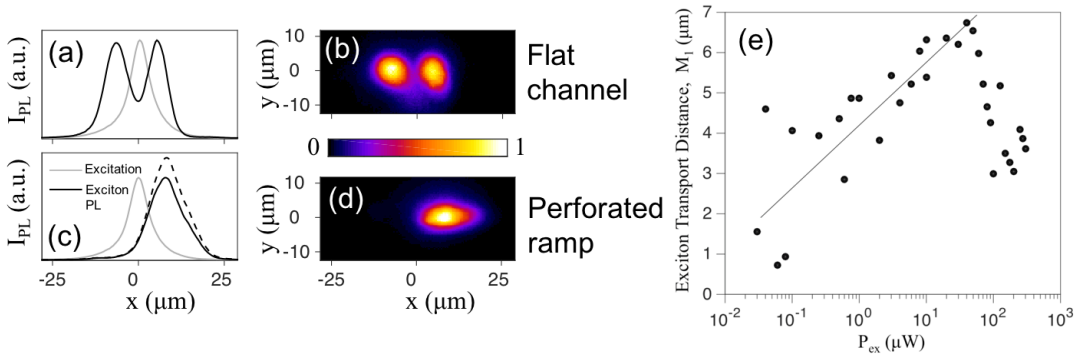

Figure 4.4: (a) IX PL profile (black) in a channel with constant potential energy formed by flat channel (electrode of constant density of 5 μm wide). Laser excitation profile (gray). (b) Image of IX PL intensity in the flat channel. Symmetric transport is observed. (c) IX PL profile (solid black) in the ramp. Laser excitation profile (gray). Estimation of IX PL profile (dashed black) with correction for the electrode transparency. (d) Image of IX PL intensity in the ramp. For all data, the laser excitation is centered around x, $y = 0$, $P_{\mathrm{ex}} = 10\ \mu$W. (e) IX transport distance down the ramp as measured by first moment of transport as a function of laser excitation power. $T_{\mathrm{bath}} = 1.8$ K, and $V = 5$ V.

4.4 Simulations

Transport in the perforated ramp device was simulated as a smooth potential energy gradient fitted to that generated by the device. The deviations due to the perforations from a completely smooth ramp potential are small compared to the disorder in the sample and can therefore be neglected in this way. To model the IX transport, a drift-diffusion equation is solved for the IX density, n_{x}:

$$\frac{\partial n_{\mathrm{x}}}{\partial t} = \nabla\left[D_{\mathrm{x}}\nabla n_{\mathrm{x}} + \mu_{\mathrm{x}} n_{\mathrm{x}} \nabla\left(u_0 n_{\mathrm{x}} + U_{\mathrm{ramp}}\right)\right] - \frac{n_{\mathrm{x}}}{\tau_{\mathrm{opt}}} + \Lambda. \tag{4.1}$$

The IX density n_{x} is constant in y and use $\nabla = \partial/\partial x$, approximately matching the geometry of the ramp as described above. The first term in the equation (4.1) represents IX diffusion. The diffusion coefficient, D_{x}, accounts for the screening of the intrinsic QW disorder potential by repulsively interacting IXs and is given by the thermionic model, $D_{\mathrm{x}} = D_{\mathrm{x}0} e^{-U_0/(u_0 n_{\mathrm{x}} + k_{\mathrm{B}} T)}$. $U_0/2 = 0.75\,\mathrm{meV}$ is the amplitude of the disorder potential and T is the exciton temperature. The

exciton-exciton interaction potential is approximated by $u_0 n_x$ with $u_0 = 4\pi d e^2/\varepsilon_b$ where ε_b is the background dielectric constant and $d = 11.5\,\text{nm}$ is the static dipole moment, corresponding to the center to center distance of the QWs. [9, 21, 92]

The second term in equation (4.1) represents IX drift. This term includes the exciton-exciton interactions and the ramp potential, $U_{\text{ramp}} = -edF_z$. A generalized Einstein relationship defines the IX mobility, $\mu_x = D_x(e^{T_0/T} - 1)/(k_B T_0)$ where $T_0 = (\pi\hbar^2 n_x)/(2M_x k_B)$ is the temperature of quantum degeneracy. The exciton generation rate, Λ, has a Gaussian profile with a width equal to the width of the laser excitation spot. τ_{opt} is the IX optical lifetime and takes into account that only low energy excitons inside the light cone may couple to light [8].

An IX thermalization equation is solved, which gives a calculation of the IX temperature T:

$$\frac{\partial T}{\partial t} = S_{\text{pump}}(T_0, T, \Lambda, E_i) - S_{\text{phonon}}(T_0, T). \tag{4.2}$$

Here, S_{pump} is the heating due to the laser excitation which is characterized by the excess energy of photo-excited excitons, $E_i = 17\,\text{meV}$. S_{phonon} describes cooling of IXs via the emission of bulk longitudinal acoustic phonons. The model parameters and more details of the calculation of S_{pump}, S_{phonon} and τ_{opt} can be found in Refs. [22, 9, 21]. The coupled equations (4.1-4.2) describing the IX transport and thermalization kinetics are integrated in time until steady state solutions are obtained. The IX PL intensity is then calculated from the IX decay rate, taking into account the aperture angle of the CCD in the experiment.

Figure 4.5 summarized the results of the simulations. Figure 4.5(a) shows the calculated IX density and PL intensity profiles. The laser profile is shown in grey, the IX density is in black, and the IX PL is in red. The IX density and PL profiles are qualitatively different due to IX heating from the laser excitation, see Section 1.3. Figure 4.5(b) shows this enhancement of the IX temperature in the excitation spot.The directed control of transport down the ramp is in agreement with the experimental images in Figure 4.4(a).

Figure 4.5(d) shows the bare ramp potential U_{ramp} in black and the ramp potential with

screening effects from the exciton-exciton repulsion taken into account $U_{\text{ramp}} + u_0 n_{\text{x}}$ in red, compare to experimental screened ramp potential measured and plotted in Figure 4.3(d).

Figures 4.5(c), 4(e), and 4(f) show the IX drift velocity, diffusion coefficient, and mobility, respectively. Their values are comparable to those for IX transport in devices where no electrode perforation is involved [21, 22, 35, 29], indicating that the perforations do not cause additional substantial obstacles for IX transport.

Figure 4.5(g) shows the average transport distance of IXs along the ramp M_1 as a function of exciton generation rate $\Lambda_0 = \Lambda(x = 0)$. The units of Λ_0 in Figure 4.5(g) can be transformed to the excitation power: $P_{\text{ex}} \sim \Lambda_0 A_{\text{ex}} E_{\text{ex}}/\alpha$, where A_{ex} is the excitation spot area, E_{ex} is the energy of a photon in the laser excitation, and α is an assumed IX-excitation probability per photon. The qualitative similarities between this model and the experimental data (compare Figure 4.5(g) and Figure 4.4(b)) further confirms that variations in the ramp potential due to the electrode perforations are small enough to not inhibit the mobility of IXs. We note that this model gives a nonlinear increase of the IX transport distance with IX density (Figure 4.5(g)). This is mainly due to the nonlinear dependence of the IX diffusion coefficient on IX density, $D_{\text{x}} = D_{\text{x}}(n_{\text{x}})$, given above.

4.5 Acknowledgements

The text of chapter 4, in part, is a reprint of the material as it appears in C. J. Dorow, Y. Y. Kuznetsova, J. R. Leonard, M. K. Chu, L. V. Butov, J. Wilkes, M. Hanson, and A. C. Gossard, Indirect excitons in a potential energy landscape created by a perforated electrode. *Applied Physics Letters* 108, 073502 (2016), ©2016 AIP Publishing LLC, where the dissertation author was the first author. The co-authors in these publications directed, supervised, and co-worked on the research which forms the basis of this chapter.

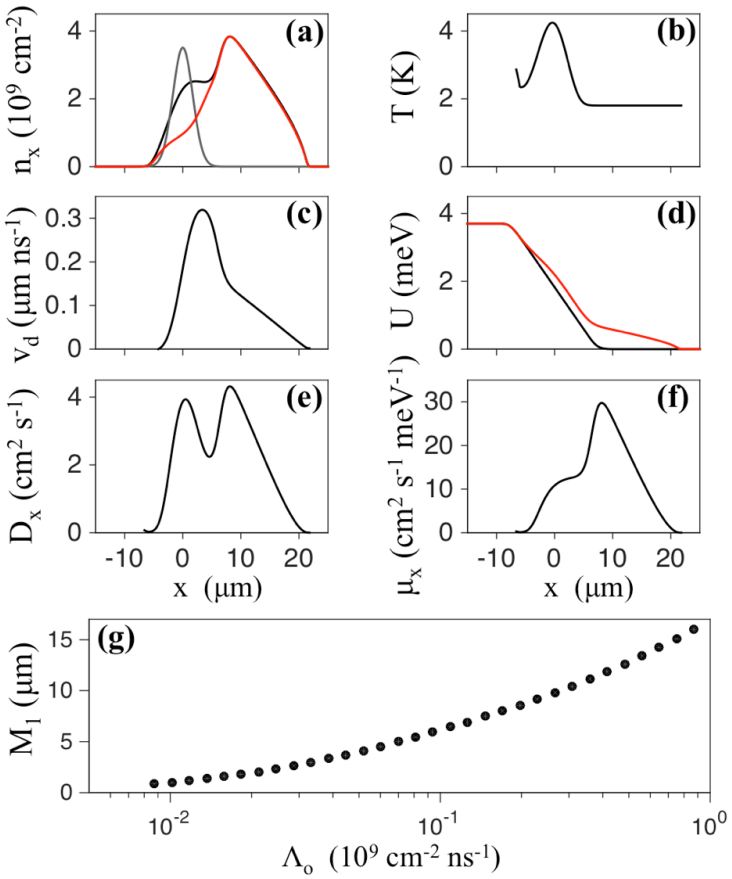

Figure 4.5: Results of theoretical simulations. (a) IX density (black), IX PL intensity (red), and laser excitation profile (gray). (b) IX temperature. (c) IX drift velocity. (d) Ramp potential (black) and effective IX potential (red) due to the ramp potential plus screening from the exciton-exciton repulsive interaction. (e) IX diffusion coefficient. (f) IX mobility. $\Lambda_o = 0.23 \times 10^9$ cm^{-2}ns^{-1} and $T_{bath} = 1.8$ K for simulations (a-f). (g) The average IX transport distance along the ramp as a function of exciton generation rate Λ_o. $T_{bath} = 1.8$ K.

Chapter 5

Excitonic Split-Gate Device

The aim of the work presented in this chapter is to open the field of IXs to mesoscopics. Mesoscopic physics occurs at intermediate length scales and is the regime where quantum mechanical effects begin to play a role and the wave nature of particles becomes relevant. We have chosen to pursue the split-gate device as a first step toward excitonic mesoscopic devices.

5.1 Introduction to split-gate devices

A split-gate device is a device which forms a narrow constriction or narrow channel for particle transport. Split-gates are ofter referred to as "quantum point contacts." Split-gates developed for electrons have resulted in many interesting observations including electron focusing [93, 94, 95, 96], conductance quantization [97, 98], electron beam collimation [99, 100, 101], and electron flow branching [102, 103]. In this chapter, we present the first realization of an excitonic split-gate device.

5.2 Excitonic split-gate device design and fabrication

The excitonic split-gate is composed of two electrodes: one large background electrode (blue in Figure 5.1(a)) which achieves the IX regime with application of V_e, and split-gate "arms" (grey in Figure 5.1(a)) which directly control the width of the spit-gate constriction by varying V_g.

The split-gate device was fabricated on a CQW structure with an n^+ GaAs layer with n_{Si} = 10^{18} cm^{-3} which serves as a homogeneous ground plane electrode. Two 8 nm GaAs QWs with a 4 nm $Al_{0.33}Ga_{0.67}As$ barrier are positioned 100 nm above the n^+ GaAs layer inside an undoped 1 μm thick $Al_{0.33}Ga_{0.67}As$ layer. The top semi-transparent electrodes are fabricated by depositing 2 nm Ti and 7 nm Pt with electron beam evaporation.

Simulations shown in Figure 5.1(b) show the ability to control the width of the spit-gate constriction by varying V_g on the split-gate electrode. Figure 5.1(c) is the extracted constriction width for different IX energies. This split-gate design allows the width of the constriction to vary over the span of 2 μm. Figure 5.1(d) and (e) show the simulated split-gate bare potential profile and the resulting IX PL.

5.3 Experimental results

The characterization of the excitonic split-gate device is presented in Figure 5.2. Figure 5.2(a) shows a subset of IX PL images where the split-gate arms are outlined in white dashed lines. IXs were photo-generated with a 633 nm HeNe laser focused to a spot with a full width half maximum of 5 μm centered around x = 0 and y = -5 μm. It was observed that IX flux through the constriction can be controlled in two ways: by varying V_{g} or P_{ex}.

The two columns of Figure 5.2(a) are images taken with a narrower constriction width (V_{g} = +4.5 V) and a wider constriction width (V_{g} = +5.5 V). The wider constriction width results in a large IX flux through the split-gate constriction. The IX flux through the constriction is shown to increase with V_{g} in Figure 5.2(b) and (d) for several laser excitation powers.

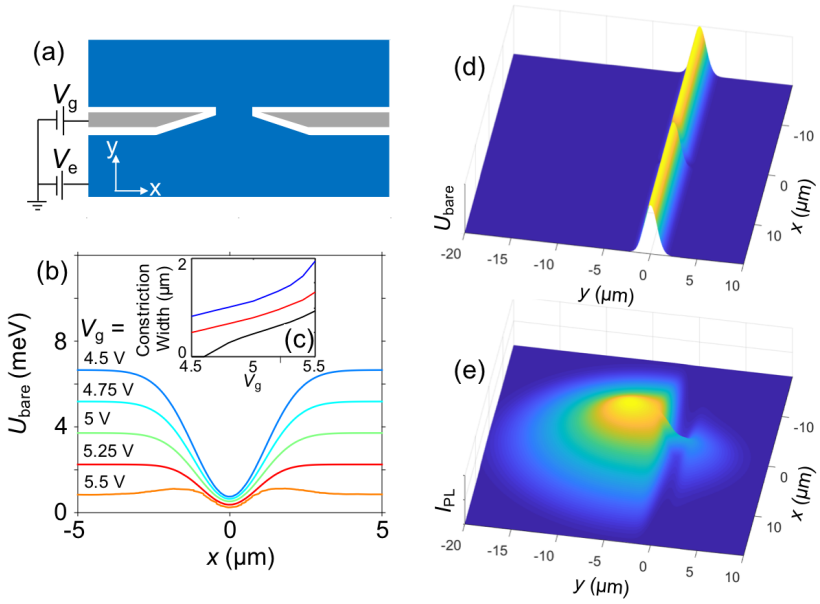

Figure 5.1: (a) Schematic of split-gate device. Arm electrodes in gray control constriction width. (b) Simulated bare constriction potential energy profiles for different split-gate voltages V_g for fixed voltage on the large electrode (blue in (a)), V_e = 5.5 V. (c) Extracted corresponding constriction width w for IXs with different energies of E = 0.5 (black), 0.7 (red), and 1 meV (blue) vs V_g. (d) Simulated IX potential energy profile in the bare, unscreened split-gate device. (e) Simulated IX PL in the potential of (d).

Additionally, the two rows of Figure 5.2(a) are images taken at different laser excitation powers, P_{ex} = 5 μW and 100 μW. It is observed that higher laser excitation power results in higher IX flux through the constriction, even with V_g (and therefore constriction width) held constant. This effect is presented in Figure 5.2(c) which shows IX PL profile (integrated over x) for different laser excitation powers and Figure 5.2(e) which shows IX flux vs. P_{ex}. The IX flux through the constriction increases with increasing P_{ex} because of the more efficient disorder screening at higher IX densities, stemming from the IX repulsive interactions.

This proof-of-principle experiment presented in this section is performed with a T_{bath} =1.7 K, which is in the diffusive regime of transport characterized as when the mean free path is small compared to the device dimensions. Simulations of IX transport in the split-gate device in the diffusive regime were performed, and the results are presented in Section 5.4.

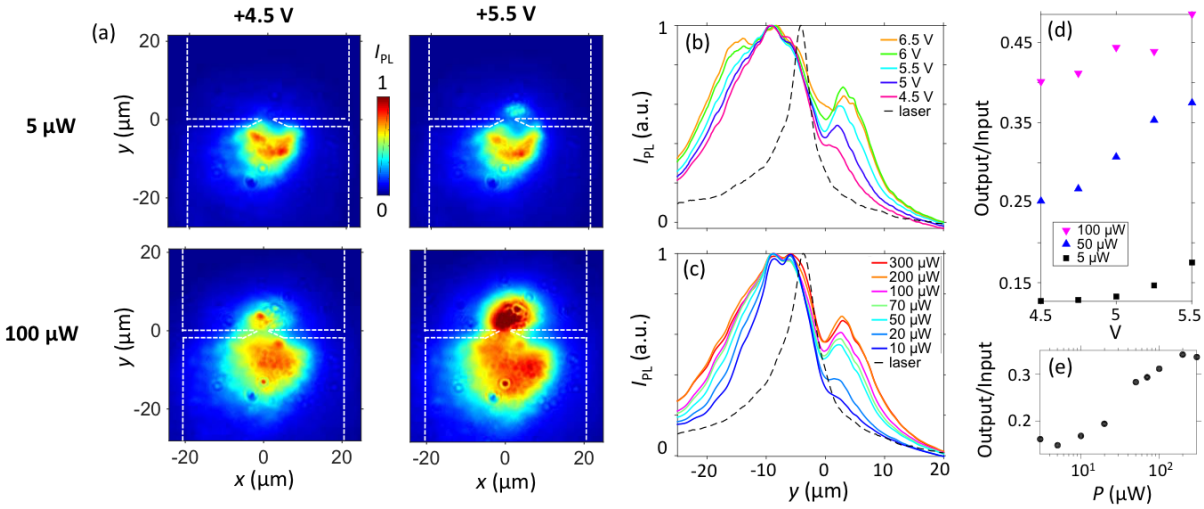

Figure 5.2: (a) IX PL images of IXs in the split-gate device for P_{ex} = 5 μW and 100 μW and V_g = +4.5 V and +5.5 V. The laser excitation is centered around x = 0 and y = -5 μm. White lines outline split-gate device arms. (b) Profile of IX PL integrated over all x for several V_g with P_{ex} = 50 μW. Laser excitation profile shown in black dashed line. (c) Profile of IX PL integrated over all x for several P_{ex} at V_g = 4.5 V. Laser excitation profile shown in black dashed line. (d) IX flux through constriction vs V_g for several laser excitation powers. (e) IX flux through constriction vs P_{ex} at V_g = 4.5 V. The large electrode is held at V_e = 5.5 V for all data.

5.4 Simulations

The following nonlinear partial differential equation was used to model IX transport through the split-gate:

$$\nabla \cdot [D\nabla n + \mu n \nabla (u_0 n + U_{\text{bare}})] + \Lambda_0 - \frac{n}{\tau} = 0. \tag{5.1}$$

The first term in square brackets in Equation 1 accounts for IX diffusion, n is the IX density, D the IX diffusion coefficient. The second term accounts for IX drift due to the dipole-dipole IX interaction, which is approximated by the plate capacitor formula $u_0 n = \frac{4\pi e^2 d}{\varepsilon} n$, ε is the dielectric constant [9], and due to the split-gate potential $U_{\text{bare}}(x,y) = -edF_z(x,y)$. The IX mobility μ is given by the Einstein relation $\mu = D/(k_B T)$. The effect of in-plane disorder intrinsic to QWs is approximated using a "thermionic model" for the diffusion coefficient,

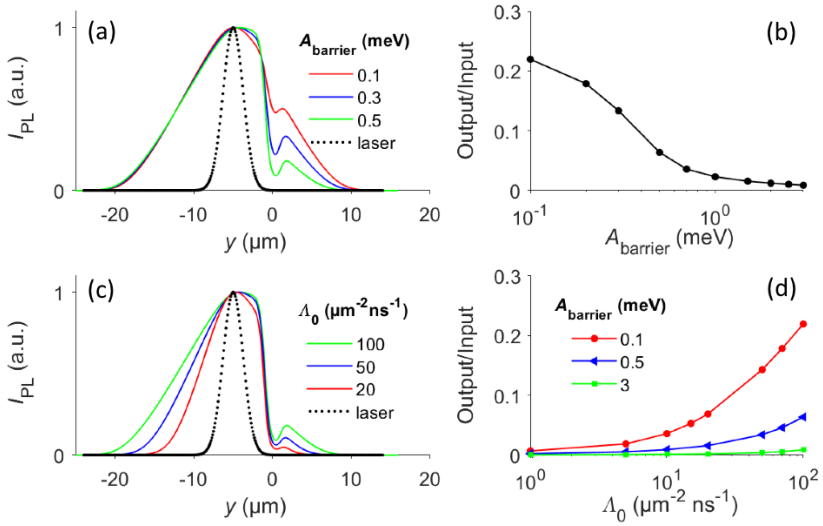

Figure 5.3: Simulations of IX transport through the split-gate. (a) IX PL vs bare barrier height, A_{barrier}. IX generation rate γ_0 = 100 $\mu m^{-2} ns^{-1}$. IX PL is integrated over x. The laser profile is shown with black dashed line. Simulated results correspond to experimental data: V_g = 5.7 V (A_{barrier} = 0.1 meV), V_g = 5.66 V (A_{barrier} = 0.3 meV), and V_g = 5.63 V (A_{barrier} = 0.5 meV). (b) IX flux through constriction vs A_{barrier}, generation rate γ_0 = 100 $\mu m^{-2} ns^{-1}$. (c) IX PL vs. γ_0 with A_{barrier} = 0.5 meV. IX PL is integrated over x. (d) IX flux through constriction vs γ_0. A_{barrier} = 0.1, 0.5, and 3 meV. For all simulations, T_{bath} =1.7 K.

$D = D^{(0)} \exp\left(-U_{\text{dis}}/(k_B T + u_0 n)\right)$ [9]. $D^{(0)}$ is the diffusion coefficient in the absence of QW disorder and $U_{\text{dis}}/2$ is the amplitude of the disorder potential. The temperature of IXs T is approximated as $T = T_{\text{bath}}$. The non-resonant photoexcitation causes heating of the IX gas by a few Kelvin. However, the hot IXs cool to the lattice temperature within few microns of the excitation spot [22] justifying the approximation. The last two terms in Equation 1 account for the creation and decay of IXs. $\Lambda_0(x,y)$ is the IX generation rate and τ is the IX lifetime.

The simulations qualitatively reproduce the control of IX transport through the split-gate constriction by voltage V_g (compare Figure 5.2(b) and (d) with Figure 5.3(a-b)) and by laser excitation power P_{ex} (compare Figure 5.2(c) and (e) with Figure 5.3(c-d)).

5.5 Future work and acknowledgements

The realization of the excitonic split-gate presented in this chapter paves the way toward studying the quantum ballistic transport in the mesoscopic regime for cold bosons. For low temperatures (T = 100 mK, achievable IXs in dilution refrigerators), the IX coherence length can reach 10 μm, which exceeds the dimensions of the split-gate channel, the exciton inter-particle separation (0.1 μm for typical density 10^{10} cm^{-2}), and the exciton thermal de Broglie wavelength (0.5 μm for exciton temperature T = 0.1 K). These length scales indicate the feasibility of realizing IX quantum ballistic transport through excitonic split-gate devices, which will be the subject for future work.

The text of chapter 5, in part, is a reprint of the material as it appears in C. J. Dorow, J. R. Leonard, M. M. Fogler, L. V. Butov, K. W. West, and L. N. Pfeiffer, Split-gate device for indirect excitons, *Applied Physics Letters* 112, 183501 (2018), ©2018 AIP Publishing LLC, where the dissertation author was the first author. The co-authors in these publications directed, supervised, and co-worked on the research which forms the basis of this chapter.

Chapter 6

High-mobility Excitons in a Wide Single Quantum Well

6.1 Introduction to wide single quantum wells

There is a large effort to improve the mobility of IXs. Increased IX mobility leads to enhanced IX device performance and enables fundamental studies of IX transport and phenomena in low-disorder systems. In this chapter, a wide single qauntum well (WSQW) structure is employed to achieve higher IX mobility. The WSQW structure achieves a lower in-plane disorder than the CQW structure in the following way. The IX energy in the quantum well structure scales with the QW width L roughly as $1/L^2$, so random QW width fluctuations cause a smaller disorder in a wider QW.

6.2 Wide single quantum well structure

To explore IXs in WSQW structures, a WSQW sample (energy band diagram shown in Figure 1) grown by molecular beam epitaxy was used. An n^+ GaAs layer with $n_{\mathrm{Si}} = 10^{18}$ cm^{-3}

is used as a bottom electrode. One single 35 nm GaAs QW is positioned 0.2 μm above the n^+ GaAs layer within an undoped 1 μm thick $Al_{0.3}Ga_{0.7}As$ layer. The WSQW is positioned closer to the homogeneous bottom electrode to suppress the fringing in-plane electric field F_r in excitonic devices [49]. Otherwise, a high F_r could lead to IX dissociation [56]. Large electrodes were fabricated to be used to achieve the IX regime. The semitransparent electrode is fabricated by depositing 2 nm Ti and 7 nm Pt with electron beam evaporation.

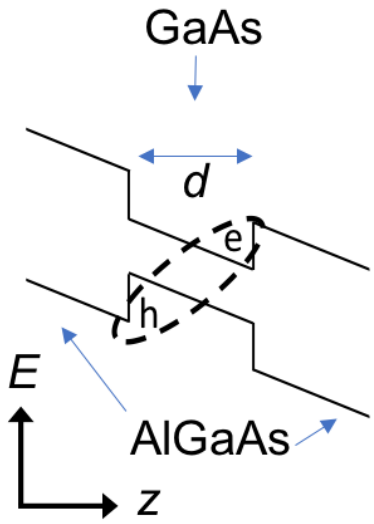

Figure 6.1: Energy band diagram of wide single quantum well structure. For the sample studied, $d \sim 19$ nm.

6.3 Indirect excitons in a wide single quantum well

The successful realization of excitonic devices requires the following properties:

i. IX energy is controllable by voltage.

ii. IX recombination rate is controllable by voltage and long IX lifetimes are achieved.

iii. Long-range IX transport over lengths exceeding the in-plane dimensions of excitonic devices is achieved.

This section shows results of experiments that demonstrate all three properties, proving that WSQW structures are valid for the development of excitonic devices. For all data of Figure 2 (cw experiments), a HeNe laser with wavelength of 633 nm is focused to a spot of HWHM = 7 μm and is centered at $x = 0$.

Figure 6.2(a) demonstrates control of IX energy by voltage. The spectra in Figure 6.2(a) are integrated over all x. Figure 6.2(b) shows the peak energy as a function of gate voltage for two excitation powers. A fit to the energy shift vs. gate voltage gives an estimate of the effective quantum well width, or e and h separation d, to be about 19 nm. It is also observed that there is a small blue shift in peak energy with increasing laser power. This blue shift demonstrates the dipolar nature of the IX and occurs due to the repulsive interactions of the oriented dipoles.

Figure 6.2(c) shows the spectra at V_g = -4 V for several excitation powers. The spectra is integrated over all x. An increase in linewidth and a blue shift in energy is observed with increasing laser excitation power, which corresponds to increasing IX density. As mentioned above, the blue shift at higher powers is due to the repulsive interactions of IXs due to being oriented dipoles. The IX linewidth increase with increasing density is due to interaction induced broadening [43].

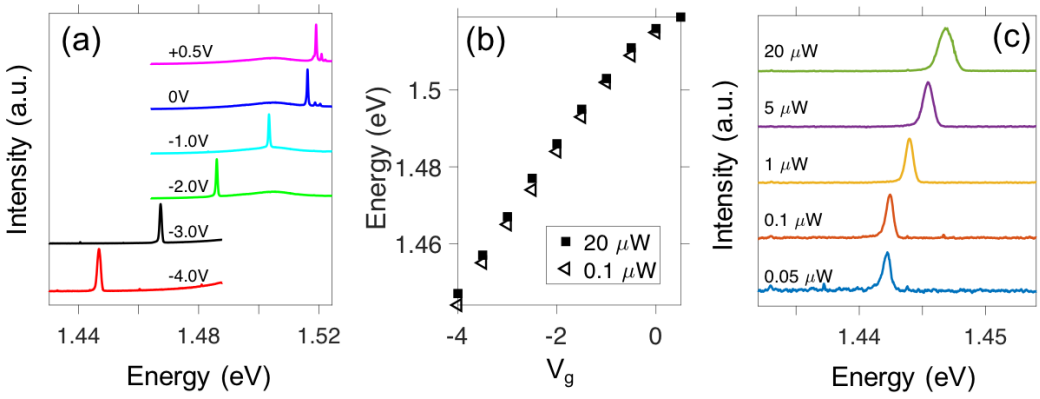

Figure 6.2: (a) IX PL spectra vs voltage V_g for laser excitation power $P_{ex} = 20$ μW. (b) IX energy vs V_g for $P_{ex} = 0.1$ and 20 μW. (c) IX spectrum vs P_{ex} for $V_g = -4$ V. All spectra are spatially integrated.

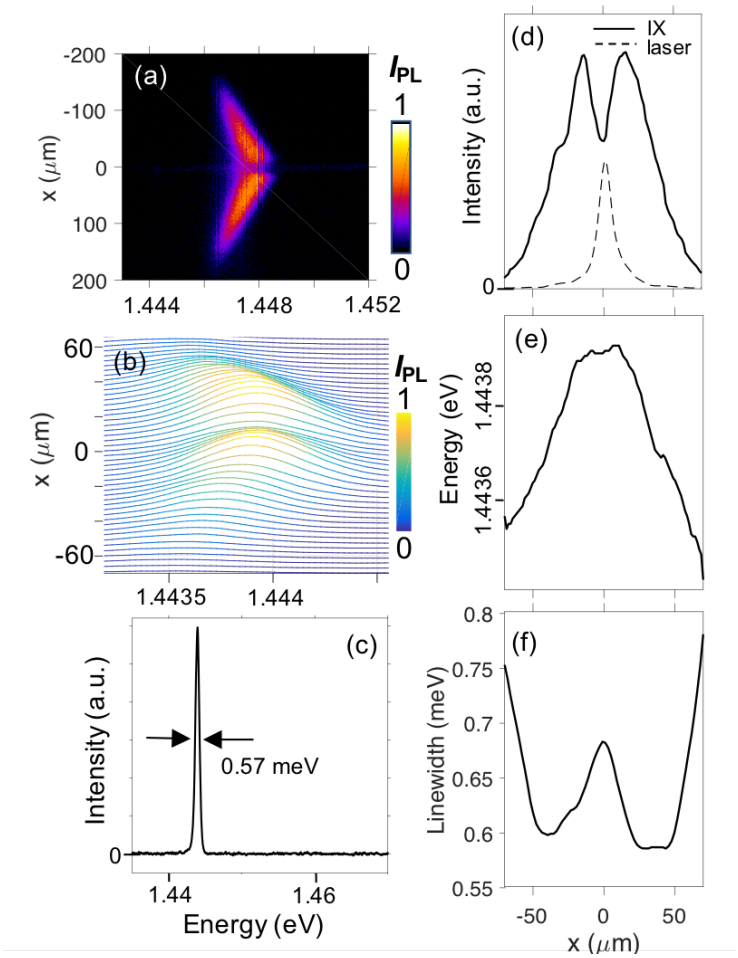

Figure 6.3: (a) x-energy IX PL pattern with cw excitation. $P_{ex} = 20$ μW and $V_g = -4$ V. (b) The spatial dependence of IX PL spectrum at $P_{ex} = 1$ μW and $V_g = -4$ V. (c) IX PL spectrum at $x = 30$ μm from (b) with linewidth of 0.57 meV. (d) Spectrally integrated IX emission intensity (laser excitation profile is shown as dashed line), (e) IX emission energy, and (f) IX emission linewidth.

Figure 6.3(a) shows the x-energy image of the IX PL. Long-range IX transport is observed here as the IX PL extends far beyond that laser excitation spot, as seen in Figure 6.3(d). The IX PL emission forms a ring shape, which is the inner ring in the IX PL emission pattern as described in Section 1.3. To better show the spectral profile of the IX PL, waterfall cuts are shown in Figure 6.3(b) for $P_{ex} = 1$ μW and $V_g = -4$ V. A record narrow IX PL linewidth is extracted from Figure 6.3(b) at x = 30 μm and is presented in Figure 6.3(c), where the linewidth is measured to be 0.57 meV. This record narrow linewidth is resultant of a low in-plane disorder of the WSQW.

The IX emission energy and the IX linewidth as a function of radius are presented in Figure 6.3(e) and (f) respectively. The IX linewidth is non-monotonic with radius, stemming from effects of IX interaction and disorder [43]. Near the excitation spot, the IX density is high and the IX linewidth is larger due to higher interaction-induced broadening and higher IX temperatures. Away from the excitation spot, the IX density is lower and the IX linewidth is larger due to less efficient screening of the in-plane QW disorder by the IXs, giving higher disorder-induced broadening.

6.4 Time-resolved imaging and measurement of the diffusion coefficient in a wide single quantum well

In order to directly measure transport of IXs in the WSQW and to study IX diffusion coefficient and lifetime, time-resolved optical imaging was performed. IXs were generated using a 640 nm semiconductor laser driven by a signal generator with a pulse duration of τ_{width} = 2000 ns and a pulse period of τ_{pulse} = 6000 ns and an edge sharpness of 1 ns as shown in Figure 6.4(a). This pulse duration and period were chosen as such to allow for the IX PL images to reach equilibrium during the laser excitation and fully decay between laser pulses. The laser was focused to a R_0 = 5 μm HWHM spot. The PL images were integrated over short, 5 ns windows (δt = 5 ns) and were taken for delay times t after the onset of the laser pulse, defined such that delay time t corresponds to an image taken during time t - δt to t. The PL images were captured with a PicoStar HR TauTec time-gated intensifier. All measurements were performed at T_{bath} = 1.7 K.

Figure 6.4 outlines the results of the time-resolved imaging. Figure 6.4(c) shows the x-energy IX PL images taken for several different delay times, showing the IX cloud evolution over time. Analysis of the images in Figure 6.4(c) are presented in Figure 6.4(d) in which the radius (which is characterized by the HWHM of the spectrally integrated IX emission) squared

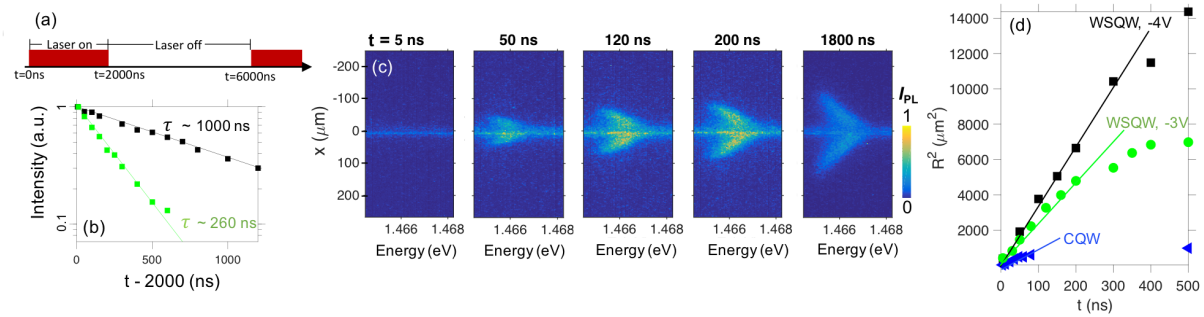

Figure 6.4: (a) Schematic of the rectangular laser excitation pulse profile. Time $t = 0$ is onset of the laser pulse. (b) Normalized total IX PL intensity (integrated over x and energy) vs t after laser pulse termination for $V_g = -4$ V (squares) and -3 V (dots). The corresponding IX lifetimes are 1000 ns and 260 ns, respectively. (c) x-energy IX PL images taken during the laser excitation pulse for several delay times t after the pulse onset. Each image is integrated over a time window of $\delta t = 5$ ns. Laser excitation spot with HWHM $R_0 = 5$ μm is centered around $x = 0$. (d) The square of HWHM of IX cloud presenting the IX transport radius R^2 vs delay time t for $V_g = -4$ V (squares) and -3 V (points). Similar data for IXs in CQW from Ref. [105] are shown by triangles for comparison. Average $P_{ex} = 30$ μW for WSQW data.

of the IX transport versus time is plotted. In Figure 6.4(d), data is shown for two samples for comparison. Firstly, the WSQW sample is presented at two different V_g (black squares and green circles), and secondly, an earlier CQW sample (blue triangles) [105] is shown for comparison. It is observed that at the short delay times, R^2 grows nearly linearly with time t. Fitting to the slope by $R^2 \sim R_0^2 + D^* t$ (solid lines in Figure 6.4(d)) gives an estimate of the IX diffusion $D^* = 350$ cm^{2}s^{-1} for IXs in WSQW for $V_g = 4$ V and 300 cm^{2}s^{-1} for $V_g = 3$ V. A similar estimate for IXs in the earlier CQW sample give 90 cm^{2}s^{-1} [105]. The IX diffusion coefficient in WSQW is roughly three times higher than in CQW studied earlier.

The high diffusion coefficient D corresponds to a high IX mobility μ_X, which is estimated by the Einstein relation $\mu = D/(k_B T)$, where k_B is the Boltzmann constant. For $T = 1.7$ K, the exciton diffusion coefficient $D = 300$ cm^{2}s^{-1} corresponds to the exciton mobility $\mu_X = 2 * 10^6$ cm^2/(eV s).

The IX lifetime in the WSQW samples is also studied via time-resolved imaging. Figure 6.4(b) shows the normalized total IX PL intensity (integrated over all x and energy) vs t after laser

pulse termination for $V_g = -4$ V (squares) and -3 V (circles). The lifetimes can be extracted by fitting to these decay curves, and the corresponding IX lifetimes are 1000 ns and 260 ns, for $V_g = -4$ V and -3 V respectively. These data demonstrate that the IXs in the WSQW have long and voltage controllable lifetimes.

In conclusion, the results included in this chapter show that WSQW heterostructures provide a platform for studying basic properties of IXs in low-disorder environments and for the development of high-mobility excitonic devices.

6.5 Acknowledgements

The text of chapter 6, in part, is a reprint of the material as it appears in C. J. Dorow, M. W. Hasling, D. J. Choksy, J. R. Leonard, L. V. Butov, K. W. West, and L. N. Pfeiffer, High-mobility indirect excitons in wide single quantum well, *Applied Physics Letters* 113, 212102 (2018), ©2018 AIP Publishing LLC, where the dissertation author was the first author. The co-authors in these publications directed, supervised, and co-worked on the research which forms the basis of this chapter.

Bibliography

[1] J. Frenkel. On the Transformation of light into Heat in Solids. I, *Physical Review* 37, 17 (1931)

[2] J. Frenkel. On the Transformation of Light into Heat in Solids. II, *Physical Review* 37, 1276 (1931)

[3] A. A. High, J. R. Leonard, A. T. Hammack, M. M. Fogler, L. V. Butov, A. V. Kavokin, K. L. Campman, and A. C. Gossard. Spontaneous coherence in a cold exciton gas, *Nature* 483, 584 (2012)

[4] L. V. Butov. Excitonic Devices, *Superlattices Microstructures* 108, 2 (2017)

[5] L. V. Butov, A. A. Shashkin, V. T. Dolgopolov, K. L. Campman and A. C. Gossard. Magneto-optics of the spatially separated electron and hole layers in GaAs/$Al_xGa_{1-x}As$ coupled quantum wells. *Physical Review B* 60, 8753 (1999)

[6] L. V. Butov. Condensation and pattern formation in cold exciton gases in coupled quantum wells. *Journal of Physics: Condensed Matter* 16, R1577R1613 (2004)

[7] A. Alexandrou, J. A. Kash, E. E. Mendez, M. Zachau, J. M. Hong, T. Fukuzawa, Y. Hase. Electric-field effects on exciton lifetimes in symmetric coupled GaAs/$Al_{0.3}Ga_{0.7}As$ double quantum wells. *Physical Review B* 42, 9225(1990)

[8] L.C. Andreani, F. Tassone, and F. Bassani. Radiative lifetime of free excitons in quantum wells. *Solid State Communications* 77, 641 - 645 (1991)

[9] A.L. Ivanov. Quantum diffusion of dipole-oriented indirect excitons in coupled quantum wells. *Europhysics Letters* 59, 586 - 591 (2002)

[10] M. Hagn, A. Zrenner, G. Böhm, and G. Weimann. Electric-field-induced exciton transport in coupled quantum well structures. *Applied Physics Letters* 67, 232 - 234 (1995)

[11] L.V. Butov and A.I. Filin. Anomalous transport and luminescence of indirect excitons in AlAs/GaAs coupled quantum wells as evidence for exciton condensation. *Physical Review B* 58 1980-2000, (1998)

[12] A.V. Larionov, V.B. Timofeev, J. Hvam, and K. Soerensen. Interwell excitons in GaAs/AlGaAs double quantum wells and their collective properties. *Journal of Experimental and Theoretical Physics* 90 1093-1104, (2000)

[13] D. A. B. Miller, D. S. Chemla, T. C. Damen, A. C. Gossard, W. Wiegmann, T. H. Wood, C. A. Burrus. *Physical Review B* 32, 1043 (1985)

[14] H. J. Polland, L. Schultheis, J. Kuhl, E. O. Göbel, C. W. Tu. *Physical Review Letters* 55, 2610 (1985)

[15] A. Gärtner, A. W. Holleitner, J. P. Kotthaus, and D. Schuh. Drift mobility of long-living excitons in coupled GaAs quantum wells. *Applied Physics Letters* 89, 052108 (2006)

[16] S. G. Tikhodeev. On the Bose-Einstein condensation of particles with finite lifetime - as demonstrated by excitons. *Solid State Communications* 72, 1075-1079 (1989)

[17] A. L. Ivanov, C. Ell, and H. Haug. Phonon-assisted Boltzmann kinetics of a Bose gas: Generic solution for $T \leq T_c$. *Physical Review E* 55, 6363 (1997)

[18] A. L. Ivanov, P. B. Littlewood, and H. Haug. Bose-Einstein statistics in thermalization and photoluminescence of quantum-well excitons. *Physical Review B* 59, 5032 (1999)

[19] L. V. Butov, C. W. Lai, D. S. Chemla, Yu. E. Lozovik, K. L. Campman, and A. C. Gossard. Observation of magnetically induced effective mass enhancement of quasi 2D excitons. *Physical Review Letters* 87, 216804 (2001)

[20] L. V. Butov, A. C. Gossard, and D. S. Chemla. Macroscopically ordered state in an exciton system. *Nature* 418, 751 - 754 (2002)

[21] A. L. Ivanov, L. E. Smallwood, A. T. Hammack, S. Yang, L. V. Butov, and A. C. Gossard. Origin of the inner ring in photoluminescence patterns of quantum well excitons. *Europhysics Letters* 73, 920 - 926 (2006)

[22] A. T. Hammack, L. V. Butov, J. Wilkes, L. Mouchliadis, E. A. Muljarov, A. L. Ivanov, and A. C. Gossard. Kinetics of the inner ring in the exciton emission pattern in coupled GaAs quantum wells. *Physical Review B* 80, 155331 (2009)

[23] L. V. Butov, L. S. Levitov, A. V. Mintsev, B. D. Simons, A. C. Gossard, and D. S. Chemla. Formation mechanism and low-temperature instability of exciton rings. *Physical Review Letters* 92, 117404 (2004)

[24] R. Rapaport, G. Chen, D. Snoke, S. H. Simon, L. Pfeiffer, K. West, Y. Liu, and S. Denev. Charge separation of dense two-dimensional electron-hole gases: mechanism for exciton ring pattern formation. *Physical Review Letters* 92(11), 117405 (2004)

[25] M. Haque. Ring-shaped luminescence pattern in biased quantum wells studied as a steady-state reaction front. *Physical Review E* 73(6), 066207 (2006)

[26] S. Yang, L. V. Butov, L. S. Levitov, B. D. Simons, and A. C. Gossard. Exciton front propagation in photoexcited GaAs quantum wells. *Physical Review B* 81, 115320 (2010)

[27] L. S. Levitov, B. D. Simons, and L. V. Butov. Pattern formation as a signature of quantum degeneracy in a cold exciton system. *Physical Review Letters* 94, 176404 (2005)

[28] Y. Y. Kuznetsova, J. R. Leonard, L. V. Butov, J. Wilkes, E. A. Muljarov, K. L. Campman, and A. C. Gossard. Excitation energy dependence of the exciton inner ring. *Physical Review B* 85, 165452 (2012)

[29] P. Andreakou, S. V. Poltavtsev, J. R. Leonard, E. V. Calman, M. Remeika, Y. Y. Kuznetsova, L. V. Butov, J. Wilkes, M. Hanson, A. C. Gossard. Optically controlled excitonic transistor. *Applied Physics Letters* 104, 091101 (2014)

[30] Y. Y. Kuznetsova, M. Remeika, A. A. High, A. T. Hammack, L. V. Butov, M. Hanson, and A. C. Gossard. All-optical excitonic transistor. *Optics Letters* 35, 1587 - 1589 (2010)

[31] G. Grosso, J. Graves, A. T. Hammack, A. A. High, L. V. Butov, M. Hanson and A. C. Gossard. Excitonic switches operating at around 100 K. *Nature Photonics* 3, 577 - 580 (2009)

[32] A. A. High, A. T. Hammack, L. V. Butov, and A. C. Gossard. Exciton optoelectronic transistor. *Optics Letters* 32, 2466 - 2468 (2007)

[33] Sen Yang, A. T. Hammack, M. M. Fogler, L. V. Butov, A. C. Gossard. Coherence Length of Cold Exciton Gases in Coupled Quantum Wells. *Physical Review Letters* 97, 187402 (2006)

[34] C. J. Dorow, Y. Y. Kuznetsova, J. R. Leonard, M. K. Chu, L. V. Butov, J. Wilkes, M. Hanson, A. C. Gossard. Indirect excitons in a potential energy landscape created by a perforated electrode. *Applied Physics Letters* 108, 073502 (2016)

[35] J. R. Leonard, M. Remeika, M. K. Chu, Y. Y. Kuznetsova, A. A. High, L. V. Butov, J. Wilkes, M. Hanson and A. C. Gossard. Transport of Indirect Excitons in a Potential Energy Gradient. *Applied Physics Letters* 100, 231106 (2012)

[36] A. G. Winbow, L. V. Butov, and A. C. Gossard. Photon storage with sub-nanosecond readout rise time in coupled quantum wells. *Journal of Applied Physics* 104, 063515 (2008)

[37] A. G. Winbow, A. T. Hammack, L. V. Butov, and A. C. Gossard. Photon Storage with Nanosecond Switching in Coupled Quantum Well Nanostructures. *Nano Letters* 7, 1349 - 1351 (2007)

[38] A. A. High, E. E. Novitskaya, L. V. Butov, and A. C. Gossard. Control of Exciton Fluxes in an Excitonic Integrated Circuit. *Science* 321, 229 - 231 (2008)

[39] E. V. Calman, M. M. Fogler, L. V. Butov, S. Hu, A. Mishchenko, A. K. Geim. Indirect excitons in van der Waals heterostructures at room temperature. *Nature Communications* 9, 1895 (2018)

[40] E. V. Calman, C. J. Dorow, M. M. Fogler, L. V. Butov, S. Hu, A. Mishchenko, A. K. Geim. Control of excitons in multi-layer van der Waals heterostructures. *Applied Physics Letters* 108, 101901 (2016)

[41] M. M. Fogler, L. V. Butov, K. S. Novoselov. High-temperature superfluidity with indirect excitons in van der Waals heterostructures. *Nature Communications* 5, 4555 (2014)

[42] A. K. Geim and I. V. Grigorieva. Van der Waals heterostructures. *Nature* 499, 419 - 425 (2013)

[43] A. A. High, A. T. Hammack, L. V. Butov, L. Mouchliadis, A. L. Ivanov, M. Hanson, and A. C. Gossard. Indirect excitons in elevated traps. *Nano Letters* 9, 2094 (2009)

[44] A. A. High, A. K. Thomas, G. Grosso, M. Remeika, A. T. Hammack, A. D. Meyertholen, M. M. Fogler, L. V. Butov, M. Hanson, and A. C. Gossard. Trapping Indirect Excitons in a GaAs Quantum-Well Structure with a Diamond-Shaped Electrostatic Trap. *Physical Review Letters* 103, 087403 (2009)

[45] A.A. High, J.R. Leonard, M. Remeika, L.V. Butov, M. Hanson, A.C. Gossard. Condensation of excitons in a trap. *Nano Letters* 12, 2605-2609 (2012)

[46] Y. Y. Kuznetsova, P. Andreakou, M. W. Hasling, J. R. Leonard, E. V. Calman, L. V. Butov, M. Hanson, and A. C. Gossard. Two-dimensional snowflake trap for indirect excitons. *Optics Letters* 40, 589 (2015)

[47] T. Huber, A. Zrenner, W. Wegscheider, M. Bichler. Electrostatic Exciton Traps. *Physica Status Solidi A* 166, R5 (1998)

[48] A. V. Gorbunov, V. B. Timofeev. Interwell excitons in a lateral potential well in an inhomogeneous electric field. *Journal of Experimental and Theoretical Physics Letters* 80, 185 (2004)

[49] A. T. Hammack, N. A. Gippius, S. Yang, G. O. Andreev, L. V. Butov, M. Hanson, A. C. Gossard. Excitons in electrostatic traps. *Journal of Applied Physics* 99, 066104 (2006)

[50] G. Chen, R. Rapaport, L. N. Pffeifer, K. West, P. M. Platzman, S. Simon, Z. Vörös, D. Snoke. *Physical Review B* 74, 045309 (2006)

[51] G. J. Schinner, J. Repp, E. Schubert, A. K. Rai, D. Reuter, A. D. Wieck, A. O. Govorov, A. W. Holleitner, J. P. Kotthaus. Confinement and Interaction of Single Indirect Excitons in a Voltage-Controlled Trap Formed Inside Double InGaAs Quantum Wells. *Physical Review Letters* 110, 127403 (2013)

[52] Y. Shilo, K. Cohen, B. Laikhtman, K. West, L. Pfeiffer, R. Rapaport. Particle correlations and evidence for dark state condensation in a cold dipolar exciton fluid. *Nature Communications* 4, 2335 (2013)

[53] Y. Mazuz-Harpaz, K. Cohen, B. Laikhtman, R. Rapaport, K. West, L. N. Pfeiffer. Radiative lifetimes of dipolar excitons in double quantum wells. *Physical Review B* 95, 155302 (2017)

[54] A.T. Hammack, M. Griswold, L.V. Butov, L.E. Smallwood, A.L. Ivanov, and A.C. Gossard. Trapping of Cold Excitons in Quantum Well Structures with Laser Light. *Physical Review Letters* 96, 227402 (2006)

[55] M. W. Hasling, Y. Y. Kuznetsova, P. Andreakou, J. R. Leonard, E. V. Calman, C. J. Dorow, L. V. Butov, M. Hanson, A. C. Gossard. Stirring potential for indirect excitons. *Journal of Applied Physics* 117, 023108 (2015)

[56] S. Zimmermann, A. O. Govorov, W. Hansen, J. P. Kotthaus, M. Bichler, and W. Wegscheider. Lateral superlattices as voltage-controlled traps for excitons. *Physical Review B* 56, 13414 (1997)

[57] S. Zimmermann, G. Schedelbeck, A. O. Govorov, A. Wixforth, J. P. Kotthaus, M. Bichler, W. Wegscheider, G. Abstreiter. Spatially resolved exciton trapping in a voltage-controlled lateral superlattice. *Applied Physics Letters* 73, 154 (1998)

[58] M. Remeika, J. C. Graves, A. T. Hammack, A. D. Meyertholen, M. M. Fogler, and L. V. Butov, M. Hanson and A. C. Gossard. Localization-Delocalization Transition of Indirect Excitons in Lateral Electrostatic Lattices. *Physical Review Letters* 102, 186803 (2009)

[59] M. Remeika, M. M. Fogler, L. V. Butov, M. Hanson, and A. C. Gossard. Two-dimensional electrostatic lattices for indirect excitons. *Applied Physics Letters* 100, 061103 (2012)

[60] M. Remeika, J. R. Leonard, C. J. Dorow, M. M. Fogler, L. V. Butov, M. Hanson, and A. C. Gossard. Measurement of exciton correlations using electrostatic lattices. *Physical Review B* 92, 115311 (2015)

[61] A. G. Winbow, J. R. Leonard, M. Remeika, Y. Y. Kuznetsova, A. A. High, A. T. Hammack, L. V. Butov, J. Wilkes, A. A. Guenther, A. L. Ivanov, M. Hanson and A. C. Gossard. Electrostatic Conveyer for Excitons. *Physical Review Letters* 106, 196806 (2011)

[62] K. W. Madison, F. Chevy, W. Wohlleben, and J. Dalibard. Vortex Formation in a Stirred Bose-Einstein Condensate. *Physical Review Letters* 84, 806 (2000)

[63] J. R. Abo-Shaeer, C. Raman, J. M. Vogels, and W. Ketterle. Observation of vortex lattices in Bose-Einstein condensates. *Science* 292, 476 (2001)

[64] V. Schweikhard, I. Coddington, P. Engels, V. P. Mogendorff, and E. A. Cornell. Rapidly Rotating Bose-Einstein Condensates in and near the Lowest Landau Level. *Physical Review Letters* 92, 040404 (2004)

[65] Y. J. Lin, R. L. Compton, K. Jimnez-Garca, J. V. Porto, I. B. Spielman. Synthetic magnetic fields for ultracold neutral atoms. *Nature* 462, 628 - 632 (2009)

[66] L. P. Gor'kov and I. E. Dzyaloshinskii. Contribution to the theory of the Mott exciton in a strong magnetic field. Zh. Eksp. Teor. Fiz. 53, 717 (1968)

[67] I. V. Lerner and Yu. E. Lozovik. Two-dimensional electron-hole system in a strong magnetic field as an almost ideal exciton gas. Zh. Eksp. Teor. Fiz. 78, 1167 (1980)

[68] C. Kallin and B. I. Halperin. Excitations from a filled Landau level in the two-dimensional electron gas. *Physical Review B* 30, 5655 (1984)

[69] R. J. Elliott and R. Loudon, Theory of the absorption edge in semiconductors in a high magnetic field. *Journal of Physics and Chemistry of Solids* 15, 196 (1960)

[70] D. Paquet, T. M. Rice, and K. Ueda. Two-dimensional electron-hole fluid in a strong perpendicular magnetic field: Exciton Bose condensate or maximum density two-dimensional droplet. *Physical Review B* 32, 5208 (1985)

[71] L. V. Butov, A. Zrenner, G. Abstreiter, A. V. Petinova, and K. Eberl, *Physical Review B* 52, 12153 (1995)

[72] H. Hasegawa and R. E. Howard. Optical absorption spectrum of hydrogenic atoms in a strong magnetic field. *Journal of Physics and Chemistry of Solids* 21, 179 (1961)

[73] Yu. E. Lozovik, I. V. Ovchinnikov, S. Yu. Volkov, L. V. Butov, and D. S. Chemla. Quasi-two-dimensional excitons in finite magnetic fields. *Physical Review B* 65, 235304 (2002)

[74] A. B. Dzyubenko and A. L. Yablonskii. Intrawell and interwell magnetoexcitons in $In_xGa_{1-x}As$/GaAs coupled double quantum wells. *Physical Review B* 53, 16355 (1996)

[75] L. V. Butov, A. A. Shashkin, V. T. Dolgopolov, K. L. Campman and A. C. Gossard. Magneto-optics of the spatially separated electron and hole layers in GaAs/$Al_xGa_{1-x}As$ coupled quantum wells. *Physical Review B* 60, 8753 (1999)

[76] L. V. Butov, A. Imamoglu, K. L. Campman, and A. C. Gossard. Coulomb Effects in Spatially Separated Electron and Hole Layers in Coupled Quantum Wells *Journal of Experimental and Theoretical Physics* 92, 260 (2001)

[77] K. Kowalik-Seidl, X. P. V*ö*gele, F. Seilmeier, D. Schuh, W. Wegscheider, A. W. Holleitner, and J. P. Kotthaus. Forming and confining of dipolar excitons by quantizing magnetic fields. *Physical Review B* 83, 081307(R) (2011)

[78] G. J. Schinner, J. Repp, K. Kowalik-Seidl, E. Schubert, M. P. Stallhofer, A. K. Rai, D. Reuter, A. D. Wieck, A. O. Govorov, A. W. Holleitner, and J. P. Kotthaus. Quantum Hall signatures of dipolar Mahan excitons. *Physical Review B* 87, 041303(R) (2013)

[79] Yu. E. Lozovik and A. M. Ruvinskii. Magnetoexciton absorption in coupled quantum wells. *Journal of Experimental and Theoretical Physcis* 85, 979 (1997)

[80] J. Wilkes and E. A. Muljarov. Excitons and polaritons in planar heterostructures in external-electric and magneticfields: A multi-sub-level approach. *Superlattices and Microstructures* 108, 32-41 (2017)

[81] E. Hanamura. Rapid radiative decay and enhanced optical nonlinearity of excitons in a quantum well. *Physical Review B* 38, 1228 (1988)

[82] J. Feldmann, G. Peter, E. O. Gbel, P. Dawson, K. Moore, C. Foxon, and R. J. Elliott. Linewidth dependence of radiative exciton lifetimes in quantum wells. *Physical Review Letters* 59, 2337 (1987)

[83] M. Z. Maialle, E. A. de Andrada e Silva, and L. J. Sham. Exciton spin dynamics in quantum wells. *Physical Review B* 47, 15776 (1993)

[84] L. V. Butov, V. D. Kulakovskii, and E. I. Rashba. Excitons and deexcitons in a neutral 2D magnetoplasma with an integer filling of Landau levels: Experiment and theory. *Journal of Experimental and Theoretical Physics* 53, 109 (1991)

[85] A. V. Gorbunov and V. B. Timofeev. Compensation of dipolar-exciton spin splitting in magnetic field. *Solid State Communications* 157, 6 (2013)

[86] A. A. High, A. T. Hammack, J. R. Leonard, Sen Yang, L. V. Butov, T. Ostatnicky, M. Vladimirova, A. V. Kavokin, T. C. H. Liew, K. L. Campman, and A. C. Gossard. *Physical Review Letters* 110, 246403 (2013)

[87] L. V. Butov, V. D. Kulakovskii, G. E. W. Bauer, A. Forchel, and D. Gr*ü*tzmacher. Excitons in dense two-dimensional electron-hole magnetoplasmas. *Physical Review B* 46, 12765 (1992)

[88] Y. Y. Kuznetsova, C. J. Dorow, E. V. Calman, L. V. Butov, J. Wilkes, E. A. Muljarov, K. L. Campman, and A. C. Gossard. Transport of indirect excitons in high magnetic fields. *Physical Review B* 95, 125304 (2017)

[89] J. Wilkes and E. A. Muljarov. Exciton effective mass enhancement in coupled quantum wells in electric and magnetic fields. *New Journal of Physics* 18 023032 (2016)

[90] K. Sivalertporn, L. Mouchliadis, A. L. Ivanov, R. Philp, and E. A. Muljarov. Direct and indirect excitons in semiconductor coupled quantum wells in an applied electric field. *Physical Review B* 85, 045207 (2012)

[91] Y. Y. Kuznetsova, A. A. High, and L. V. Butov. Control of excitons by laterally modulated electrode density. *Applied Physics Letters* 97, 201106 (2010)

[92] A. L. Ivanov, E. A. Muljarov, L. Mouchliadis, and R. Zimmermann. Comment on "Photoluminescence Ring Formation in Coupled Quantum Wells: Excitonic Versus Ambipolar Diffusion. *Physical Review Letters* 104, 179701 (2010)

[93] Y. V. Sharvin. A possible method for studying Fermi surfaces. *Journal of Experimental and Theoretical Physics* 48, 984 - 985 (1965)

[94] Y. V. Sharvin and L. M. Fisher. Observation of focused electron beams in a metal. *Journal of Experimental and Theoretical Physics* 1, 152 - 153 (1965)

[95] V. S. Tsoi, Focusing of electrons in a metal by a transverse magnetic field. Pisma *Journal of Experimental and Theoretical Physics* 19, 70 - 71 (1974)

[96] H. van Houten, B. J. van Wees, J. E. Mooij, C. W. J. Beenakker, J. G. Williamson, and C. T. Foxon. Coherent electron focussing in a two-dimensional electron gas. *Europhysics Letters* 5, 721 - 725 (1988)

[97] B. J. van Wees, H. van Houten, C. W. J. Beenakker, J. G. Williamson, L. P. Kouwenhoven, D. van der Marel, and C. T. Foxon. Quantized conductance of point contacts in a two-dimensional electron gas. *Physical Review Letters* 60, 848 - 850 (1988)

[98] D. A. Wharam, T. J. Thornton, R. Newbury, M. Pepper, H. Ahmed, J. E. F. Frost, D. G. Hasko, D. C. Peacockt, D. A. Ritchie, and G. A. C. Jones. One-dimensional transport and the quantisation of the ballistic resistance. *Journal of Physics C: Solid State Physics* 21, L209 - L214 (1988)

[99] L. W. Molenkamp, A. A. M. Staring, C. W. J. Beenakker, R. Eppenga, C. E. Timmering, J. G. Williamson, C. J. P. M. Harmans, and C. T. Foxon. Electron-beam collimation with a quantum point contact. *Physical Review B* 41, 1274 - 1277 (1990)

[100] M. A. Eriksson, R. G. Beck, M. Topinka, J. A. Katine, R. M. Westervelta, K. L. Campman, and A. C. Gossard. Cryogenic scanning probe characterization of semiconductor nanostructures. *Applied Physics Letters* 69, 671 - 673 (1996)

[101] R. Crook, C. G. Smith, C. H. W. Barnes, M. Y. Simmons, and D. A. Ritchie. Imaging diffraction-limited electronic collimation from a non-equilibrium one-dimensional ballistic constriction. *Journal of Physics: Condensed Matter* 12, L167 - L172 (2000)

[102] M. A. Topinka, B. J. LeRoy, S. E. J. Shaw, E. J. Heller, R. M. Westervelt, K. D. Maranowski, and A. C. Gossard. Imaging coherent electron flow from a quantum point contact. *Science* 289, 2323 - 2326 (2000)

[103] M. A. Topinka, B. J. LeRoy, R. M. Westervelt, S. E. J. Shaw, R. Fleischmann, E. J. Heller, K. D. Maranowski, and A. C. Gossard. Coherent branched flow in a two-dimensional electron gas. *Nature* 410, 183 - 188 (2001)

[104] H. L. Stormer, D. C. Tsui, and A. C. Gossard. The fractional quantum Hall effect. *Review of Modern Physics* 71, S298 (1999)

[105] C. J. Dorow, M. W. Hasling, E. V. Calman, L. V. Butov, J. Wilkes, K. L. Campman, and A. C. Gossard. Spatially resolved and time-resolved imaging of transport of indirect excitons in high magnetic fields. *Physical Review B* 95, 235308 (2017)